

1 **Rheologic constraints on the upper mantle from five years of**
2 **postseismic deformation following the El Mayor-Cucapah**
3 **earthquake**

4 **T. T. Hines¹, E. A. Hetland¹**

5 ¹Department of Earth and Environmental Sciences, University of Michigan, Ann Arbor, Michigan, USA.

6 **Key Points:**

- 7 • Transient postseismic deformation can be observed following the El Mayor-Cucapah
8 earthquake at epicentral distances of up to 400 km
9 • Near-field postseismic deformation exhibits early transience that decays to a sustained
10 rate which is elevated above the preseismic trend
11 • ~~A Far-field postseismic deformation can be explained with a Zener or Burgers upper~~
12 ~~mantle can explain far-field deformation while near-field transience can be described~~
13 ~~with afterslip rheology upper mantle~~

14 **Abstract**

15 ~~Five years of postseismic deformation following the Mw7.2~~ We analyze five years of Southern
 16 California GPS data following the ~~Mw=7.2~~ El Mayor-Cucapah earthquake reveals transient deformation
 17 that decays back to its pre-earthquake trend after about . We observed transient postseismic
 18 deformation which persists for three years at epicentral distances greater than ~ 200 km. At
 19 closer distances, the rapid In the near-field, rapid postseismic transience decays to a sustained
 20 rate which exceeds its ~~pre-earthquake preseismic~~ trend. We attempt to determine the mech-
 21 anisms driving this deformation, where we consider afterslip at seismogenic depths and vis-
 22 coelastic relaxation in the lower crust and upper mantle as candidate mechanisms. We find that
 23 early, rapid, near-field deformation can be explained with afterslip on the fault that ruptured
 24 coseismically, while the . The later, sustained, near-field deformation can be explained with
 25 either continued afterslip in an effectively elastic lower crust , or lower crustal viscoelastic relaxation
 26 viscoelastic relaxation in the lower crust with a steady-state viscosity of $\sim 10^{19}$ Pa s . The trend
 27 in and possibly continued afterslip. The later postseismic deformation in the far-field deformation
 28 is best explained with a transient viscosity of $\sim 10^{18}$ Pa s in the upper mantle. We argue that
 29 a transient rheology in the mantle is preferable over a Maxwell rheology because it better pre-
 30 dicted the decay in postseismic deformation, and also because it does not conflict with the gen-
 31 erally higher, steady-state viscosities inferred from studies of geophysical processes occurring
 32 over longer time-scales time scales.

33 **1 Introduction**

34 Ground deformation in the years following a large (~~Mw>Mw7~~) ~~earthquake provides 7~~
 35 ~~earthquake can be used to gain~~ insight into the mechanical behavior of the crust and upper man-
 36 tle. It has long been recognized that ~~The~~ interpretations of postseismic deformation can be ambiguous
 37 are not always conclusive because multiple postseismic deformation mechanisms, such as afterslip
 38 or viscoelastic relaxation in the lower crust and upper mantle, can have qualitatively similar
 39 surface expressions [e.g. Savage, 1990]. This non-uniqueness complication can potentially be
 40 remedied if the postseismic deformation occurs in an area that is sufficiently well instrumented
 41 with GPS stations [Hearn, 2003] . Owing to the dense geodetic network deployed through-
 42 out the 2000s as part of the Plate Boundary Observatory, the postseismic deformation follow-
 43 ing the April 4, 2010, ~~Mw7.2~~ ~~Mw=7.2~~ El Mayor-Cucapah earthquake in Baja California was
 44 observed at more GPS stations than any other earthquake in California to date (see Hauksson et al. [2011] and
 45 Fletcher et al. [2014] for a detailed description of this earthquake and its seismotectonic context).
 46 With such a large collection of data, we attempt to discern the mechanisms driving ~~postseismic~~
 47 ~~deformation following the El Mayor-Cucapah earthquake, where we consider both afterslip~~
 48 ~~and viscoelastic relaxation in the lower crust and upper mantle as candidate mechanisms~~
 49 ~~the postseismic deformation.~~

50 Previous studies which have modeled postseismic deformation following the El Mayor-
 51 Cucapah earthquake include Pollitz et al. [2012], Gonzalez-Ortega et al. [2014], Spinler et al.
 52 [2015], and Rollins et al. [2015]. Of these studies, Gonzalez-Ortega et al. [2014] and Rollins
 53 et al. [2015] have attempted to describe the postseismic deformation with afterslip in an elas-
 54 tic half-space. Gonzalez-Ortega et al. [2014] described five months of postseismic deforma-
 55 tion, observed by InSAR and GPS stations within ~ 50 km of the rupture, with afterslip and
 56 contraction on the coseismically ruptured fault. Gonzalez-Ortega et al. [2014] noted that their
 57 preferred model underestimated the GPS displacements for stations $\gtrsim 25$ km from the rup-
 58 ture and suggested that it could be the result of unmodeled viscoelastic relaxation. Using only
 59 continuous GPS stations, which are mostly north of the rupture zone, Rollins et al. [2015] found
 60 that three years of postseismic deformation can be adequately explained by afterslip, albeit with
 61 an implausibly large amount of slip inferred on the least constrained, southern-most fault seg-
 62 ment. Here, we suggest the afterslip inferred by Rollins et al. [2015] may have been acting as
 63 a proxy for distributed relaxation in the upper mantle.

64 *Pollitz et al.* [2012], *Rollins et al.* [2015] and *Spinler et al.* [2015] have explored viscoelastic
 65 relaxation in the lower crust and upper mantle as a potential postseismic deformation mechanism.
 66 The rheology of the crust and mantle is largely unknown and so modeling postseis-
 67 mic deformation with viscoelastic relaxation requires one to assume a rheologic model and
 68 then find the best fitting rheologic parameters. The inference of these rheologic parameters is
 69 a computationally expensive non-linear inverse problem which is typically approached with
 70 a forward modeling grid search method. Consequently, a simplified structure for the Earth must
 71 be assumed in order to minimize the number of rheologic parameters that need to be estimated.
 72 For example, it is commonly assumed that the lower crust and upper mantle are homogeneous,
 73 Maxwell viscoelastic layers, which may be too simplistic for postseismic studies [*Riva and Gov-*
 74 *ers, 2009; Hines and Hetland, 2013*]. To further reduce the dimensions of the model space,
 75 it is also necessary to make simplifying assumptions about the ~~nature~~-behavior of afterslip. For
 76 example, one can assume a frictional model for afterslip and parametrize afterslip in terms of
 77 the unknown rheologic properties of the fault [e.g. *Johnson et al.*, 2009; *Johnson and Segall,*
 78 2004]. One can also assume that afterslip does not persist for more than a few months and then
 79 model the later postseismic deformation assuming it to be the result of only viscoelastic re-
 80 laxation [e.g. *Pollitz et al.*, 2012; *Spinler et al.*, 2015]. However, ~~postseismic~~-afterslip in sim-
 81 ilar tectonic settings has been observed to persist for decades following earthquakes [*Çakir et al.*,
 82 2012; *Cetin et al.*, 2014]. Indeed, the preferred viscoelastic model from *Pollitz et al.* [2012] sig-
 83 nificantly underestimates deformation in the Imperial Valley, which could be indicative of un-
 84 modeled continued afterslip. Neglecting to allow for sustained afterslip as a postseismic mech-
 85 anism could then lead to biased inferences of viscosities.

86 In this study, we perform a kinematic inversion for fault slip, allowing it to persist through-
 87 out the postseismic period, while simultaneously estimating the viscosity of the lower crust
 88 and upper mantle. We create an initial model of the fault slip and effective viscosity neces-
 89 sary to describe early postseismic deformation using the method described in *Hines and Het-*
 90 *land* [2016]. This method ~~utilizes~~-uses a first-order approximation of surface deformation re-
 91 sulting from viscoelastic relaxation which is only applicable to the early postseismic period.
 92 In this case, our initial model describes the first 0.8 years of postseismic deformation follow-
 93 ing the El Mayor-Cucapah earthquake. We then use the inferred effective viscosity structure
 94 from the initial model to create a suite of postseismic models ~~to-explain-which we test against~~
 95 the five years of postseismic data available to date. Of the suite of models tested, we find that
 96 postseismic deformation following the El Mayor-Cucapah earthquake can be explained with
 97 a combination of afterslip on a fault segment running through the Sierra Cucapah and ~~viscoelastic~~
 98 ~~relaxation in~~ a Zener rheology ~~in the~~-upper mantle with a transient viscosity ~~that decays from~~
 99 ~~6×10^{18} Pa s to 1×10^{18} Pa s~~ at 120 km depth ~~on the order of~~ 10^{18} Pa s.

107 2 Data Processing

108 We use continuous GPS position time series provided by University Navstar Consortium
 109 (UNAVCO) for stations within a 400 km radius about the El Mayor-Cucapah epicenter. We
 110 collectively describe the coseismic and postseismic displacements resulting from the El Mayor-
 111 Cucapah earthquake as $u_{\text{post}}(t)$. We consider the GPS position time series, $u_{\text{obs}}(t)$, to be the
 112 combination of $u_{\text{post}}(t)$, secular tectonic deformation, annual and semi-annual oscillations, and
 113 coseismic offsets from significant earthquakes over the time span of this study. The June 14,
 114 2010, ~~Mw5.8~~ *Mw=5.8* Ocotillo earthquake and the Brawley swarm, which included an ~~Mw5.5~~
 115 ~~and an Mw5.4~~ *Mw=5.5* and an *Mw=5.4* event on August 26, 2012, (Figure 1), are the only
 116 earthquakes that produced noticeable displacements in any of the time series. We treat the dis-
 117 placements resulting from the Brawley swarm as a single event because the daily solutions pro-
 118 vided by UNAVCO cannot resolve the separate events. Although the Ocotillo earthquake had
 119 its own series of aftershocks [*Hauksson et al.*, 2011], neither the Ocotillo earthquake nor the
 120 Brawley swarm produced detectable postseismic deformation. We model displacements result-
 121 ing from these events with only a Heaviside function, $H(t)$, describing the coseismic offsets.
 122 We then model $u_{\text{obs}}(t)$ as

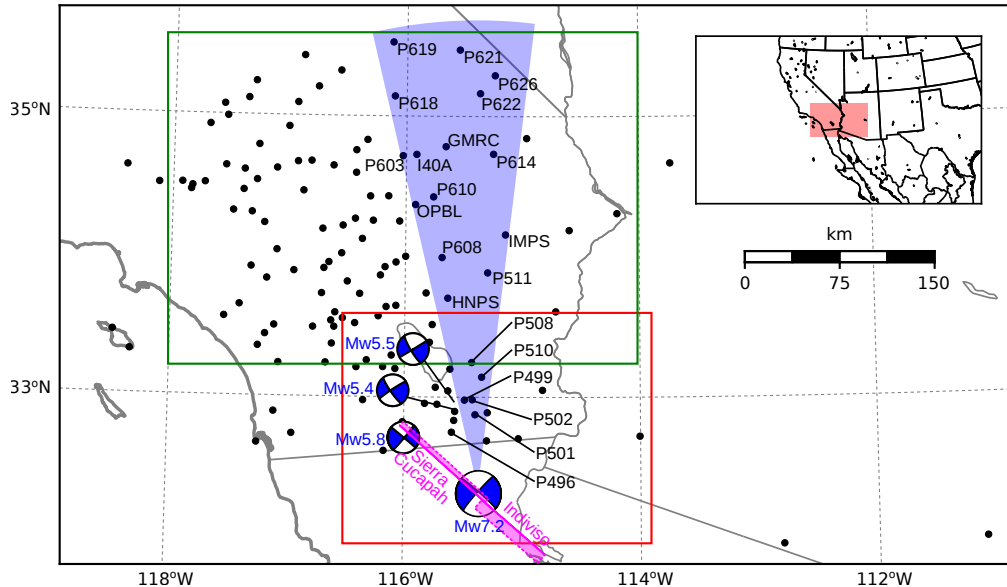


Figure 1. Map of the region considered in this study. The large focal mechanism is [the GCMT solution](#) for the El Mayor-Cucapah earthquake, and the three small focal mechanisms are for the Ocotillo earthquake and the two main shocks during the Brawley swarm. The black dots indicate the locations of GPS stations used in this study. The fault geometry used in this study is shown in [cyan-magenta](#) where dashed lines indicate buried edges of the fault segments. The green and red boxes demarcate the extent of the near-field and far-field maps (Figures 4 and 5). Stations inside the blue sector, which highlights the area within 10° of the El Mayor-Cucapah [P-axis](#), are used in Figures ??, ??-?? and ??-??.

$$u_{\text{obs}}(t) = u_{\text{pred}}(t) + \epsilon, \quad (1)$$

123 where

$$u_{\text{pred}}(t) = u_{\text{post}}(t)H(t - t_{\text{emc}}) + c_0 + c_1 t + \\ c_2 \sin(2\pi t) + c_3 \cos(2\pi t) + c_4 \sin(4\pi t) + c_5 \cos(4\pi t) + \\ c_6 H(t - t_{\text{oc}}) + c_7 H(t - t_{\text{bs}}). \quad (2)$$

In the above equations, t_{emc} , t_{oc} and t_{bs} are the times of the El Mayor-Cucapah earthquake, Ocotillo earthquake, and the Brawley swarm, respectively, c_0 through c_7 are unknown coefficients, and ϵ is the observation noise. We are using years as our unit of time which makes c_2 through c_5 the coefficients for annual and semi-annual oscillations. We only estimate jumps associated with the Ocotillo earthquake and Brawley swarm for stations within 40 km of their epicenters.

Stations which recorded displacements that clearly cannot be described by the aforementioned processes are not included in our analysis. This includes stations in the Los Angeles basin, where anthropogenic deformation can be larger than the postseismic signal that we are trying to estimate [Bawden *et al.*, 2001; Argus *et al.*, 2005]. In order to ensure an accurate estimation of the secular deformation, we only use stations that were installed at least six months prior to El Mayor-Cucapah earthquake. ~~Several even though several~~ GPS stations were installed after the ~~El-Mayor-Cucapah earthquake to improve the spatial resolution of postseismic deformation~~ [Spiner *et al.*, 2015]. Although it is difficult to get better coverage of the postseismic

138 deformation field [Spinler *et al.*, 2015]. It would be possible to subtract secular velocities de-
 139 rived from elastic block models [e.g. Meade and Hager, 2005] from velocities recorded at the
 140 newly installed stations to get an estimate of postseismic velocities, ~~we do not do so here. We~~
 141 ~~use coseismic and postseismic displacements, rather than velocities, in our inverse method described~~
 142 ~~in Section 3. We use displacements because~~ at those stations. However, estimating velocities
 143 from an already noisy displacement time series can introduce significant uncertainties depend-
 144 ing on exactly how the estimation is done. ~~We therefore use coseismic and postseismic displacements,~~
 145 ~~rather than velocities, in our inverse method described in Section 3.~~ This choice prevents us
 146 from using the newly installed stations ~~in Baja California~~ for our analysis.

147 The October 16, 1999, ~~Mw7.1~~ ~~Mw=7.1~~ Hector Mine earthquake, which occurred \sim 270
 148 km north of the El Mayor-Cucapah epicenter, produced transient postseismic deformation which
 149 we do not wish to model, either mechanically or through empirical line fitting. We thus re-
 150 strict our analysis to deformation observed six years after the Hector Mine earthquake, which
 151 is when postseismic velocities at sites ~~proximal to near~~ the Hector Mine epicenter are approx-
 152 imately constant [Savage and Svare, 2009]. When appraising our model fit in Section 3, we
 153 see some systematic residuals in the vicinity of the Hector Mine epicenter, which may be the
 154 result of errors in the assumption that the trend in Hector Mine postseismic deformation is lin-
 155 ear after six years.

156 Studies of postseismic deformation typically assume a parametric form for $u_{\text{post}}(t)$, such
 157 as one with a logarithmic or exponential time dependence [e.g. Savage *et al.*, 2005]. However,
 158 by assuming a logarithmic or exponential form of $u_{\text{post}}(t)$ we run the risk of over fitting the
 159 GPS time series and inferring a non-existent postseismic signal. We therefore do not assume
 160 any parametric form for $u_{\text{post}}(t)$ and rather treat it as integrated Brownian motion, so that

$$\dot{u}_{\text{post}}(t) = \sigma^2 \int_0^t w(s) ds, \quad (3)$$

161 where $w(t)$ is white noise and the variance of $\dot{u}_{\text{post}}(t)$ increases linearly with time by a fac-
 162 tor of σ^2 . We use a Kalman filtering approach to estimate $u_{\text{post}}(t)$ and the unknown param-
 163 eters in eq. (2). In the context of Kalman filtering, our time varying state vector is

$$\mathbf{X}(t) = [u_{\text{post}}(t), \dot{u}_{\text{post}}(t), c_0, \dots, c_7] \quad (4)$$

164 and eq. (2) is the observation function which maps the state vector to the GPS observations.
 165 We initiate the Kalman filter by assuming a prior estimate of $\mathbf{X}(t)$ at the first time epoch, de-
 166 noted $\mathbf{X}_{1|0}$, which has a sufficiently large covariance, denoted $\Sigma_{1|0}$, to effectively make our
 167 prior uninformed. For each time epoch t_i , Bayesian linear regression is used to incorporate
 168 GPS derived estimates of displacement with our prior estimate of the state $\mathbf{X}_{i|i-1}$, to form
 169 a posterior estimate of the state $\mathbf{X}_{i|i}$, which has covariance $\Sigma_{i|i}$. We then use the posterior
 170 estimate of the state at time t_i to form a prior estimate of the state at time t_{i+1} through the
 171 transition function

$$\mathbf{X}_{i+1|i} = \mathbf{F}_{i+1} \mathbf{X}_{i|i} + \delta_{i+1}, \quad (5)$$

172 where

$$\mathbf{F}_{i+1} = \begin{bmatrix} 1 & (t_{i+1} - t_i) & \mathbf{0} \\ 0 & 1 & \mathbf{0} \\ \mathbf{0} & \mathbf{0} & \mathbf{I} \end{bmatrix} \quad (6)$$

173 and δ_{i+1} is the process noise, which has zero mean and covariance described by

$$\mathbf{Q}_{i+1} = \sigma^2 \begin{bmatrix} \frac{(t_{i+1}-t_i)^3}{3} & \frac{(t_{i+1}-t_i)^2}{2} & \mathbf{0} \\ \frac{(t_{i+1}-t_i)^2}{2} & (t_{i+1}-t_i) & \mathbf{0} \\ \mathbf{0} & \mathbf{0} & \mathbf{0} \end{bmatrix}. \quad (7)$$

174 The covariance of the new prior state, $\mathbf{X}_{i+1|i}$, is then described by

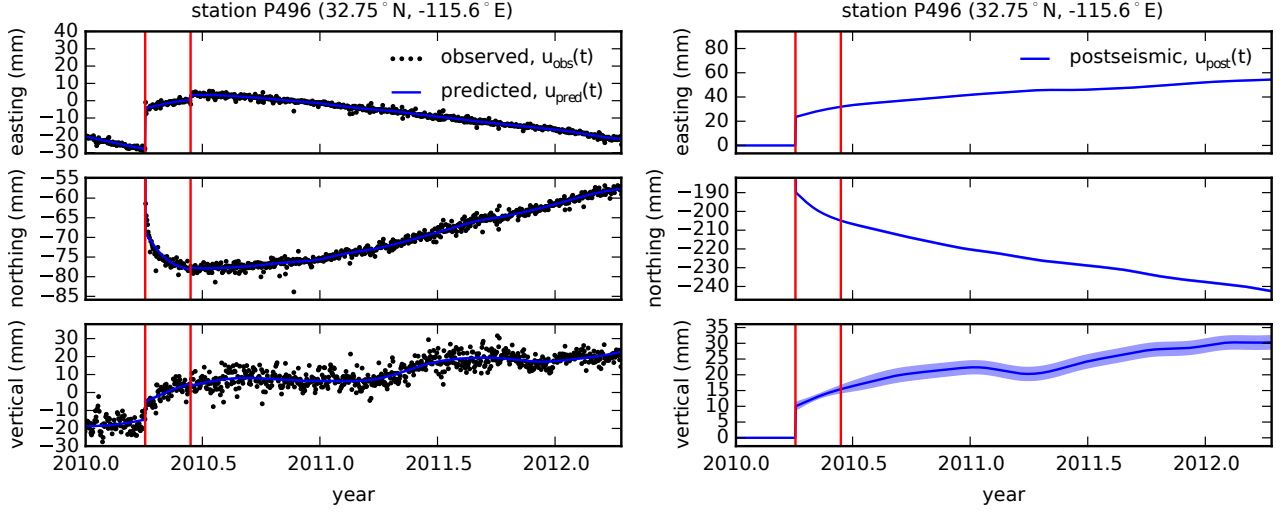
$$\Sigma_{i+1|i} = \mathbf{F}_{i+1} \Sigma_{i|i} \mathbf{F}_{i+1}^T + \mathbf{Q}_{i+1}. \quad (8)$$

175 This process is repeated for each of the N time epochs ~~at which point we~~. We then use Rauch-
 176 Tung-Striebel smoothing [Rauch *et al.*, 1965] to find $\mathbf{X}_{i|N}$, which is an estimate of the state
 177 at time t_i that incorporates GPS observation for all N time epochs. Our final estimates of $u_{\text{post}}(t)$
 178 are used in subsequent analysis, while the remaining components of the state vector are con-
 179 sidered nuisance parameters. In the interests of computational tractability, we down sample
 180 our smoothed time series from daily solutions down to weekly solutions.

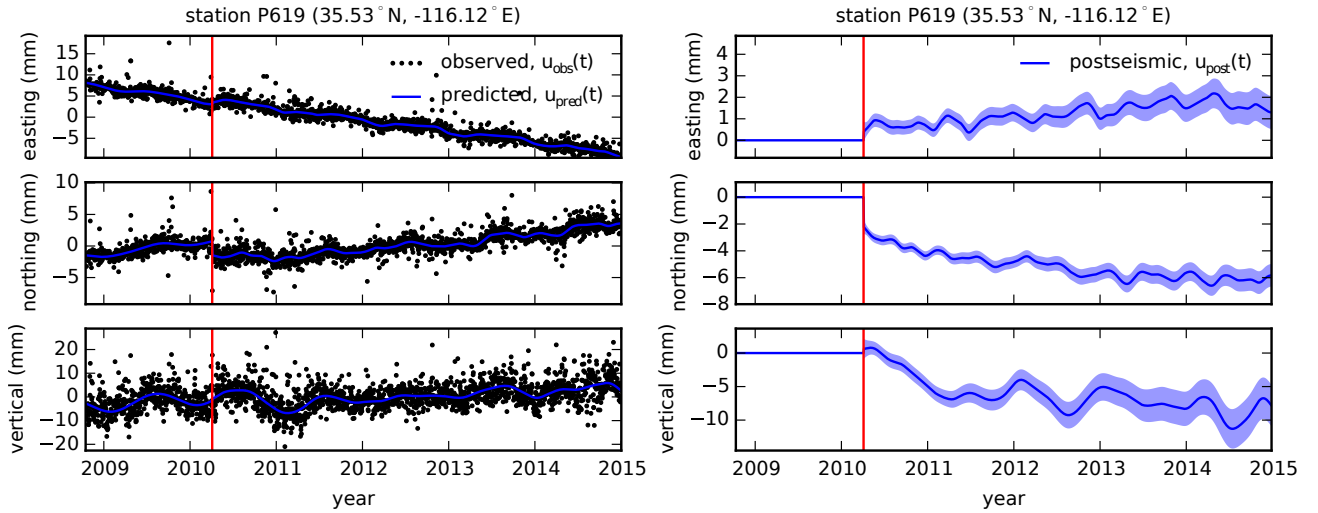
181 The smoothness of $u_{\text{post}}(t)$ is controlled by the chosen value of σ^2 , which describes how
 182 rapidly we expect postseismic displacements to vary over time. Setting σ^2 equal to zero will
 183 effectively result in modeling $u_{\text{post}}(t)$ as a straight line which is insufficient to describe the
 184 expected transient behavior in postseismic deformation. The other end member, where σ^2 is
 185 infinitely large, will result in $u_{\text{pred}}(t)$ ~~over fitting~~ overfitting the data. While one can use a max-
 186 imum likelihood based approach for picking σ^2 [e.g. Segall and Mathews, 1997], we instead
 187 take a subjective approach and choose a value for σ^2 that is just large enough to faithfully de-
 188 scribe the observed deformation at the most near-field station in our study, P496, which ex-
 189 hibits the most ~~pronounced~~ rapid changes in velocity. This ensures that σ^2 will be sufficiently
 190 large so that our estimate of $u_{\text{post}}(t)$ does not smooth out potentially valuable postseismic sig-
 191 nal at the remaining stations. We find that using $\sigma^2 = 0.05\text{m}^2/\text{yr}^3$ adequately describe all
 192 but the first week of postseismic deformation at station P496, which ~~gets incorporated into~~ slightly
 193 increases our estimate of coseismic displacements (Figure 2). We ~~assume that the first week~~
 194 ~~of deformation is overwhelmingly the result of afterslip and this afterslip is lumped into our~~
 195 ~~estimates of coseismic slip. Freed et al. (2007) noted that postseismic deformation can be observed~~
 196 ~~at distances greater than 200 km from the Hector Mine earthquake and, after filtering the time~~
 197 ~~series for stations up to 400 km from include an example of estimating $u_{\text{post}}(t)$ for a far-field~~
 198 ~~station, P619, which is about 359 km north of the El Mayor-Cucapah epicenter, we also clearly~~
 199 ~~see far-reaching postseismic transient deformation (Figure 3). At station P619, along with all~~
 200 ~~the other stations in the Mojave region, there is a south-trending postseismic transience that~~
 201 ~~persists for the first three years after the El Mayor-Cucapah earthquake. Postseismic deformation~~
 202 ~~that extends to these epicentral distances has also been observed after the Hector Mine earthquake~~
 203 ~~[Freed et al., 2007].~~

209 It is important to note that the shown uncertainties in $u_{\text{post}}(t)$ do not account for the non-
 210 negligible epistemic uncertainty in eq. (2). For example, we assume a constant rate of secu-
 211 lar deformation, which appears to be an appropriate approximation for all but perhaps the sta-
 212 tions closest to the Hector Mine epicenter, as noted above. Also, our model for seasonal de-
 213 formation in eq. (2) assumes a constant amplitude over time, which means that any yearly vari-
 214 ability in the climatic conditions could introduce systematic residuals [Davis *et al.*, 2012]. In-
 215 deed, it would be more appropriate to consider the seasonal amplitudes $c_2 - c_5$ in eq. (2) as
 216 stochastic variables [Murray and Segall, 2005]. By using constant seasonal amplitudes, our es-
 217 timate of $u_{\text{post}}(t)$ seems to describe some of the unmodeled annual and semi-annual oscilla-
 218 tions (e.g. Figure 3).

219 We show in Figures 4 and 5 the near and far-field ~~coseismic displacements and the~~ post-
 220 seismic displacements accumulated over the time intervals 0-1 years, 1-3 years, and 3-5 years,
 221 ~~as well as the coseismic displacements~~. Stations at epicentral distances beyond ~ 200 km have
 222 an elevated rate of deformation for the first three years following the earthquake. This far-field
 223 deformation ~~has a southward trend is trending southward at a rate of a few millimeters per year~~
 224 along the direction of the El Mayor-Cucapah ~~P-axis and a P-axis~~. A similar eastward trend



204 **Figure 2.** Left panels show GPS time series from UNAVCO (black)
205 and the predicted displacement (blue) from eq. (2) for a near-field station.
206 Red lines indicate the times of the El Mayor-Cucapah and Ocotillo earth-
207 quakes. The right panels show estimated coseismic and postseismic displace-
ments, u_{post} , which are extracted from the predicted displacements. The 68% confidence interval is shown in light blue.



208 **Figure 3.** same as Figure 2 but for a far-field station.

depth (km)	λ (GPa)	μ (GPa)	η_{eff} (10^{18} Pa s)	μ_k/μ
0-5	24.0	24.0	-	-
5-15	35.0	35.0	-	-
15-30	42.0	42.0	44.3	0.0
30-60	61.0	61.0	5.91	0.375
60-90	61.0	61.0	1.99	0.375
90-120	61.0	61.0	1.31	0.375
120-150	61.0	61.0	1.10	0.375
150- ∞	61.0	61.0	1.07	0.375

251 **Table 1.** Assumed and estimated material properties. λ and μ are assumed known *a priori* and are based
 252 on the values used for the coseismic model by *Wei et al.* [2011b]. The values for η_{eff} are estimated in Section
 253 3.2, and $\frac{\mu_k}{\mu}$ are the optimal shear moduli ratios found in Section 3.3 for a Zener rheology upper mantle.

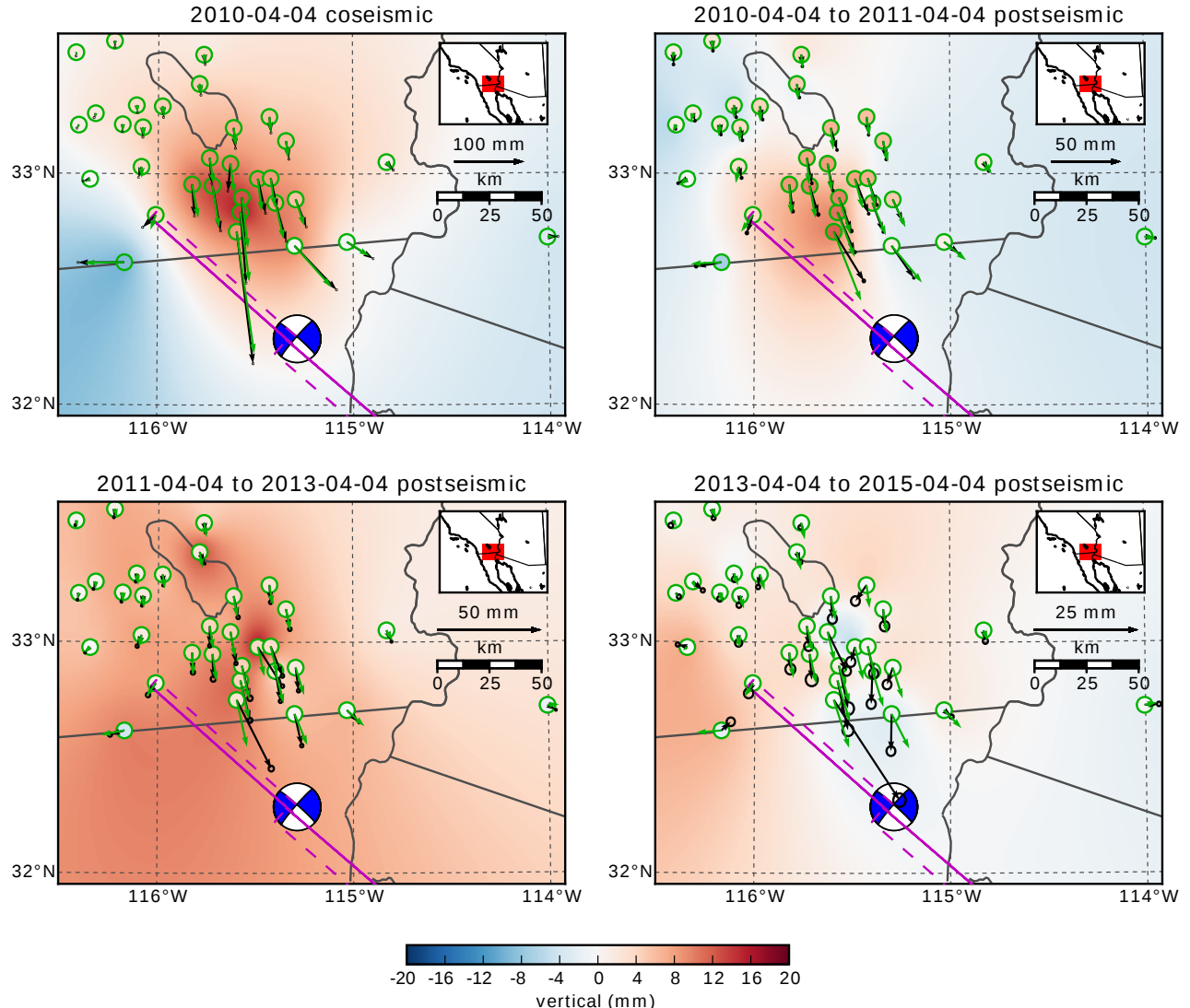
225 can be seen in the few far-field stations in Arizona, located along the ~~T-axis~~^{T-axis}. After three
 226 years, the trend in far-field postseismic deformation is barely perceptible. Most far-field sta-
 227 tions display an initial subsidence for the first year after the El Mayor-Cucapah earthquake fol-
 228 lowed by continued uplift. This trend in vertical deformation can be observed in all three of
 229 the quadrants where postseismic data is available, which means that the vertical deformation
 230 does not exhibit an anti-symmetric quadrant pattern, as would be expected for postseismic pro-
 231 cesses. Although we use vertical deformation in our analysis in Section 3, we do not put an
 232 emphasis on trying to describe the vertical deformation ~~as because~~ it likely does not have post-
 233 seismic origins.

241 The near-field postseismic deformation is notably sustained when compared to the far-
 242 field deformation. Namely, the station in this study which is closest to the El Mayor-Cucapah
 243 epicenter, P496, has ~~been moving at a steady rate~~ ~~a steady postseismic trend~~ of ~ 1.5 cm/yr
 244 to the south ~~since after~~ about one year ~~after the El Mayor-Cucapah earthquake~~. Vertical post-
 245 seismic deformation in the near-field does display a quadrant pattern which is consistent with
 246 the coseismic vertical deformation, suggesting that it is resulting from postseismic processes.
 247 However, the vertical postseismic signal is only apparent for the first year after the earthquake
 248 (Figure 4). As with the far-field deformation, there is a general trend of uplift in the near-field
 249 after about one year.

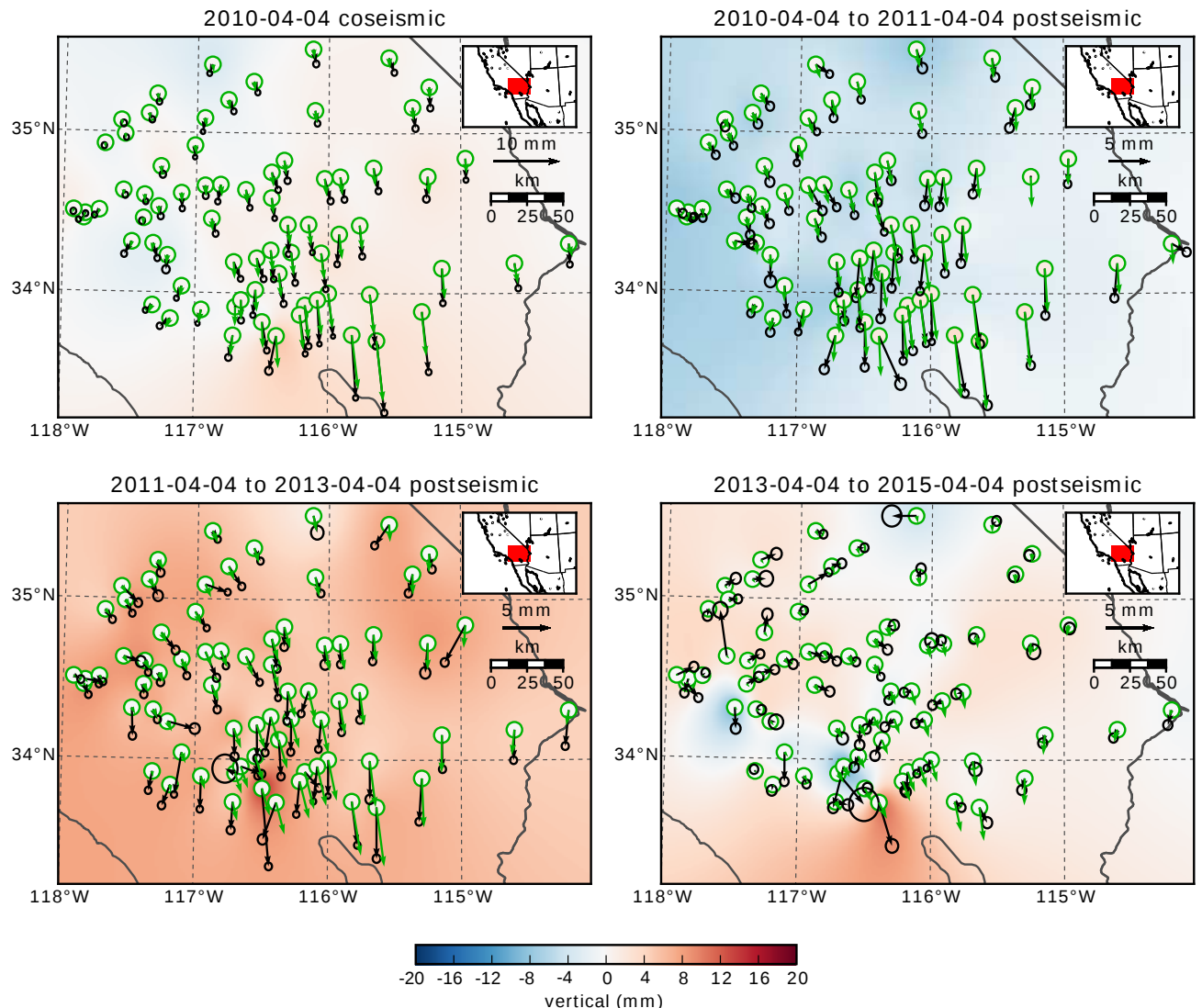
250 3 Postseismic Modeling

254 We seek to find the mechanisms driving five years of postseismic deformation follow-
 255 ing the El Mayor-Cucapah earthquake and we consider afterslip and viscoelastic relaxation as
 256 candidate mechanisms. Poroelastic rebound has also been used to model postseismic defor-
 257 mation [e.g. *Jónsson et al.*, 2003]; however, *Gonzalez-Ortega et al.* [2014] found that poroe-
 258 lastic rebound is unlikely to be a significant contributor to postseismic deformation following
 259 the El Mayor-Cucapah earthquake. Furthermore, we consider stations which are sufficiently
 260 far away from the ~~main~~-rupture that poroelastic rebound should be insignificant.

261 We estimate coseismic and time-dependent postseismic fault slip, both of which are as-
 262 sumed to occur on a fault geometry modified from *Wei et al.* [2011b]. Field studies [*Fletcher*
 263 *et al.*, 2014] and LIDAR observations [*Oskin et al.*, 2012] have revealed a significantly more
 264 complicated fault geometry than what was inferred by *Wei et al.* [2011b], especially within the
 265 Sierra Cucapah. However, we find that a relatively simple coseismic fault geometry based on
 266 [*Wei et al.*, 2011b] is adequate because most of the stations used in this study are sufficiently
 267 far from the El Mayor-Cucapah rupture ~~zone~~ that they are insensitive to the details in the fault
 268 geometry found by *Fletcher et al.* [2014] and *Oskin et al.* [2012]. The fault geometry used in
 269 this study (Figure 1) consists of the two main fault segments inferred by *Wei et al.* [2011b],



234 **Figure 4.** Near-field coseismic and cumulative postseismic displacements over the indicated time periods
 235 (black) as well as predicted displacements for our preferred model from Section 3.3 (green). The black
 236 error ellipses show the 68% confidence interval for the observed horizontal displacements. Observed vertical
 237 deformation is shown as an interpolated field and predicted vertical displacements are
 238 shown within the green circles at the base of each vector. Note that the interpolant is not well constrained in
 239 Mexico where there is no data available.

**Figure 5.** Same as Figure 4 but for far-field stations.

270 where the northern segment runs through the Sierra Cucapah up to the US-Mexico border and
 271 the southern segment is the Indiviso fault which extends down to the Gulf of California. Both
 272 segments extend from the surface to 15 km depth. We extend the northern segment by 40 km
 273 to the ~~north-west, northwest, which is~~ motivated by the clustering of aftershocks on the north-
 274 ern tip of the coseismic rupture zone [Hauksson *et al.*, 2011; Kroll *et al.*, 2013]. This extended
 275 fault segment was also found to be necessary by Rollins *et al.* [2015] and Pollitz *et al.* [2012]
 276 in order to describe the postseismic deformation.

277 3.1 Elastic Postseismic Inversion

278 We consider a variety of rheologic models for the lower crust and upper mantle. The
 279 simplest rheologic model is to consider them to be effectively elastic and isotropic. In such
 280 case, the rheologic parameters consist of the ~~reasonably well known~~ Lamé parameters, λ and
 281 μ , ~~which are reasonably well known~~ and we use the same values used by Wei *et al.* [2011b]
 282 throughout this paper (Table 31). The only unknown is the distribution of fault slip, which can
 283 be ~~easily~~-estimated from postseismic deformation through linear least squares. ~~Using~~ Rollins *et al.* [2015] used
 284 a subset of the GPS stations considered in this study, ~~Rollins *et al.* [2015]~~ and found that three
 285 years of postseismic deformation following the El Mayor-Cucapah earthquake can be explained
 286 with afterslip on the coseismic fault plane without requiring any viscoelastic relaxation. We
 287 also perform an elastic slip inversion, but we use GPS stations within a larger radius about the
 288 El Mayor-Cucapah epicenter (400 km instead of \sim 200 km). Our forward problem describing
 289 predicted postseismic deformation, u_{pred} , in terms of time dependent fault slip, s , is

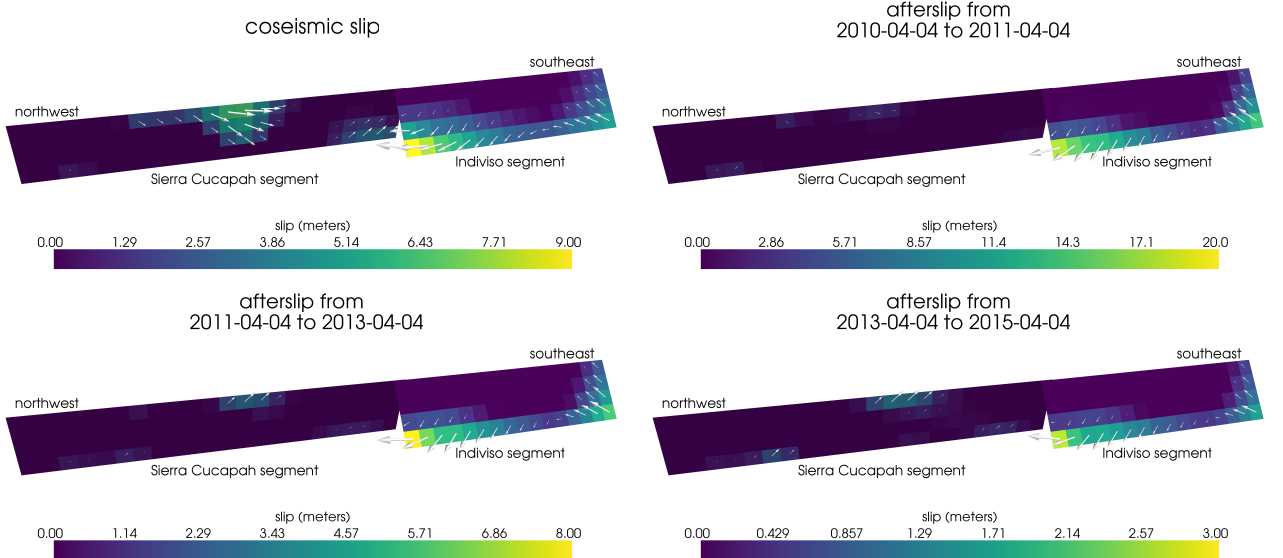
$$u_{\text{pred}}(x, t) = \int_F s(\xi, t) g(x, \xi) d\xi, \quad (9)$$

290 where F denotes the fault and $g(x, \xi)$ is the elastic Green's function describing displacement
 291 at surface position x resulting from slip at ξ on the fault. We estimate coseismic slip and the
 292 rate of afterslip ~~at the discrete time intervals~~, ~~over the postseismic time intervals~~ 0.0-0.125,
 293 0.125-0.25, ~~0.25-0.5~~, 0.5-1.0, 1.0-2.0, 2.0-3.0, 3.0-4.0, and 4.0-5.0 years ~~after the earthquake~~.
 294 Each fault segment is discretized into roughly 4 km by 4 km patches ~~and we estimate a strike-slip~~
 295 ~~and thrust component of slip for each patch. We an we~~ impose that the direction of slip and
 296 slip rate are within 45° of right-lateral. We also add zeroth-order Tikhonov regularization so
 297 that our solution for s satisfies

$$\min_s \left(\left\| \frac{u_{\text{pred}}(s) - u_{\text{post}}}{\sigma_{\text{post}}} \right\|_2^2 + \lambda_s \|s\|_2^2 \right), \quad (10)$$

298 where σ_{post} is the uncertainty on postseismic displacements and λ_s is a penalty parameter which
 299 is chosen with a trade-off curve. We use Pylith [Aagaard *et al.*, 2013] to compute the Green's
 300 functions for this inversion as well as for the remaining inversions in this paper.

301 Our coseismic slip and afterslip solutions are shown in Figure 6. ~~As with Similar to~~ Rollins
 302 *et al.* [2015], we find that a large amount of afterslip on the ~~southern Indiviso~~ fault segment
 303 is required to explain the observations. The potency of our inferred coseismic slip is $3.2 \times$
 304 10^9 m^3 , equivalent to a ~~Mw7.28~~ ~~Mw=7.28~~ earthquake when assuming a shear modulus of 32
 305 GPa. The potency of our inferred cumulative five years of afterslip is $6.1 \times 10^9 \text{ m}^3$, equiv-
 306 alent to a ~~Mw7.46~~ ~~Mw=7.46~~ earthquake, which is unrealistically large if we consider after-
 307 slip to be driven by coseismically induced stresses. Figure ??-7 shows the time series for the
 308 observed and predicted postseismic displacements at stations along the El Mayor-Cucapah ~~P~~
 309 ~~axisP-axis~~. We show the radial component of displacements with respect to the El Mayor-Cucapah
 310 epicenter and we also rescale the displacements so that the difference between the minimum
 311 and maximum observed displacements are the same for each station. Our elastic slip model
 312 accurately describes near-field postseismic deformation and systematically underestimates post-
 313 seismic deformation at epicentral distances \gtrsim 150 km. When the fault segments used in the
 314 inversion are extended down to 30 km depth, rather than 15 km, the systematic far-field resid-



318 **Figure 6.** Coseismic slip and cumulative afterslip over the indicated time intervals for when assuming the
 319 crust and mantle are elasticmodel from Section 3.1. Color indicates the magnitude of slip while and arrows
 320 indicate the motion of the hanging wall.

315 uals are smaller but remain apparent. Because an elastic model requires an unrealistic amount
 316 of afterslip and is unable to predict far-field deformation, we move on to consider viscoelas-
 317 tic models in the next section.

331 3.2 Early Postseismic Inversion

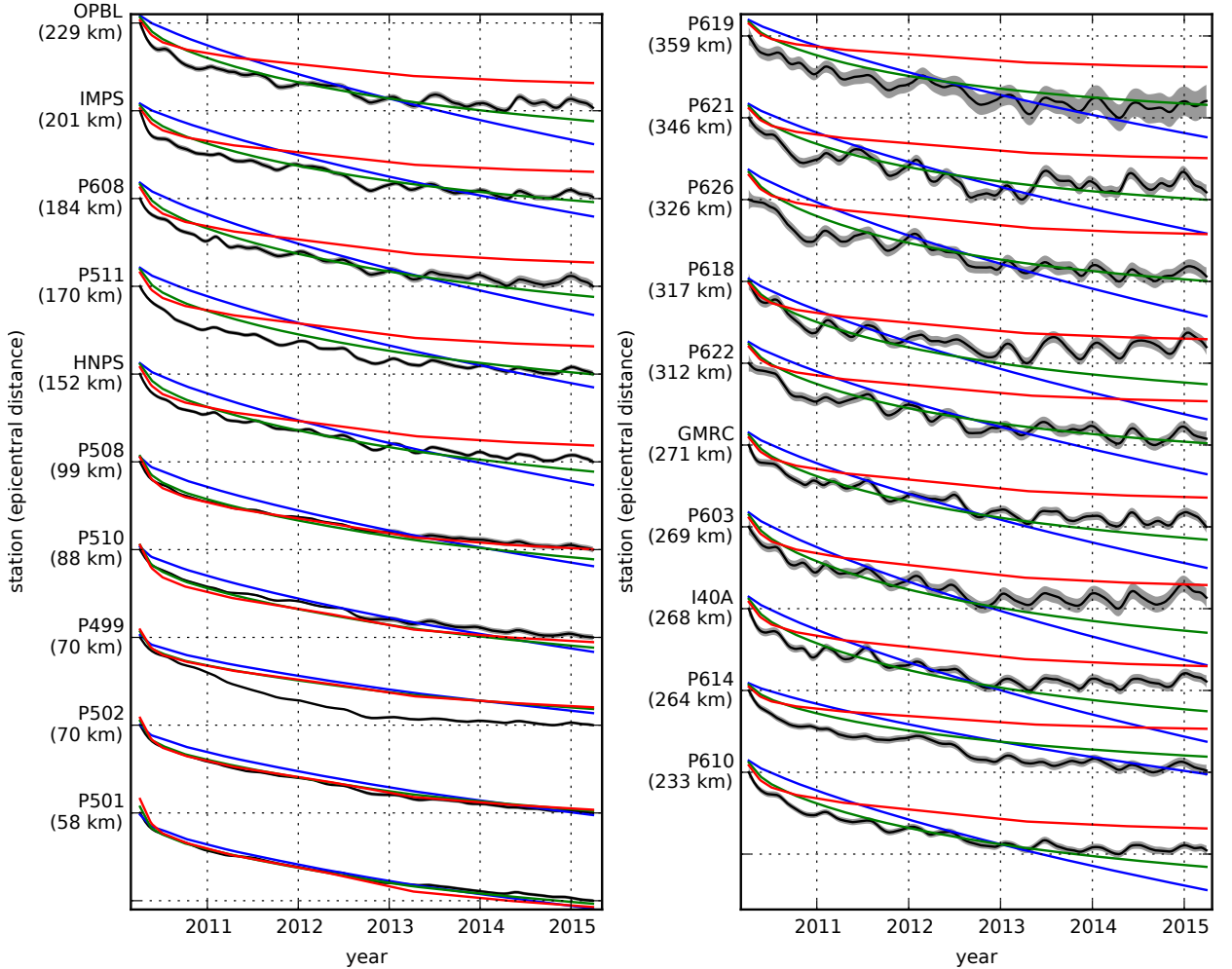
332 For any linear viscoelastic rheology of the crust and mantle, postseismic displacements
 333 resulting from time dependent fault slip can be described as

$$334 \quad u_{\text{pred}}(x, t) = \int_F s(\xi, t)g(x, \xi)d\xi + \int_0^t \int_F s(\xi, \tau)f(t - \tau, x, \xi)d\xi d\tau, \quad (11)$$

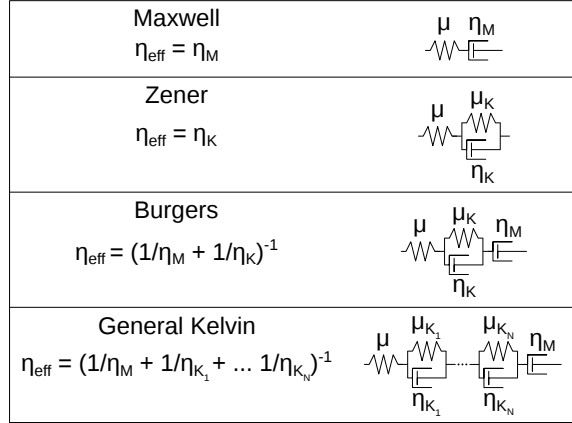
335 where $f(t, x, \xi)$ describes the time-dependent velocity at x resulting from viscoelastic relax-
 336 ation of stresses induced by slip at ξ . f is a function of λ , μ , and any additional rheologic pa-
 337 rameters controlling the viscoelastic response, which are generally not well known. Schematic
 338 representations of the viscoelastic rheologic models considered in this study are shown in Fig-
 ure 8. We discuss these rheologic models and their use in geophysical studies in Section 4.

341 In order to greatly simplify the inverse problem, we use the method described in *Hines*
 342 and *Hetland* [2016] to constrain an initial effective viscosity structure from the early postseis-
 343 mic deformation. Our method utilizesuses the fact that coseismic stresses throughout the crust
 344 and upper mantle depend on the instantaneous elastic parameters and are independent of the
 345 viscoelastic parameters which we wish to estimate. Immediately following an earthquake, each
 346 parcel will have a strain rate that is proportional to the coseismic stress and inversely propor-
 347 tional to the parcel's effective viscosity, η_{eff} . Using one-dimensional viscoelasticrheologic mod-
 348 els, we define the effective viscosity as

$$349 \quad \eta_{\text{eff}} = \left. \frac{\sigma}{\dot{\varepsilon}} \right|_{t=0}, \quad (12)$$



321 **Figure 7.** Scaled radial component of ~~observed~~ postseismic displacements u_{obs} (~~black~~) and displacements
 322 predicted by the best fitting elastic model u_{pred} (~~blue~~). Downward motion indicates that the station is
 323 moving toward the El Mayor-Cucapah epicenter. Displacement time series are scaled so that the minimum and
 324 maximum observed values lie on the grid lines. The ~~observed postseismic displacements~~, u_{post} are shown
 325 in ~~black~~ with gray indicating the 68% confidence interval. The displacements predicted by the best fitting
 326 elastic model are shown in ~~red~~. The blue and green lines are the predicted postseismic displacements for the
 327 ~~observed~~ models discussed in Section 3.3. The blue lines show the predicted displacements for the model
 328 with a Maxwell viscoelastic lower crust and upper mantle. The green line shows the predicted displacements
 329 for our preferred model, which has a Maxwell viscoelastic lower crust and a Zener viscoelastic upper mantle.
 330 The effective viscosities are the same for both models and are shown in ~~gray~~ Figure 12.



339 **Figure 8.** Schematic illustration of the rheologic models considered in this paper as well as their effective
 340 viscosities.

349 where σ is an applied stress at $t = 0$ and $\dot{\varepsilon}$ is the resulting strain rate. Figure 8 shows how
 350 η_{eff} relates to the parameters for various linear viscoelastic rheologies. We can deduce that the
 351 initial rate of surface deformation resulting from viscoelastic relaxation is a summation of the
 352 surface deformation resulting from relaxation in each parcel, scaled by the reciprocal of the
 353 parcel's effective viscosity. That is to say

$$f(0, x, \xi) = \int_L \frac{h(x, \xi, \zeta)}{\eta_{\text{eff}}(\zeta)} d\zeta, \quad (13)$$

354 where L denotes the crust and mantle and $h(x, \xi, \zeta)$ describes the initial rate of deformation
 355 resulting from viscoelastic relaxation at ζ induced by slip at ξ . We can combine eq. (13) with
 356 eq. (11) to get a first-order-first-order approximation for early postseismic deformation,

$$u_{\text{pred}}(x, t) \approx \int_F s(\xi, t) g(x, \xi) d\xi + \int_0^t \int_F \int_L \frac{s(\tau, \xi)}{\eta_{\text{eff}}(\zeta)} h(x, \xi, \zeta) d\zeta d\xi d\tau, \quad (14)$$

357 which is valid for as long as the rate of deformation resulting from viscoelastic relaxation is
 358 approximately constant. Although eq. (14) may only be valid for a short portion of the post-
 359 seismic period, its utility becomes apparent when noting that g and h are only functions of
 360 the fault geometry and instantaneous elastic properties, λ and μ , and thus g and h can be com-
 361 puted numerically as a preprocessing step. The forward problem in eq. (14) can then be rapidly
 362 evaluated for any realization of s and η_{eff} . This is in contrast to evaluating the full forward
 363 problem, eq. (11), numerically for each realization of s and the unknown rheologic prop-
 364 ties.

365 Details on how eq. (14) is used to estimate s and η_{eff} from postseismic deformation can
 366 be found in *Hines and Hetland* [2016]. A non-linear Kalman filter based inverse method can
 367 also be used to estimate s and η_{eff} in a manner akin-similar to *Segall and Mathews* [1997] or
 368 *McGuire and Segall* [2003], in which we would not have to explicitly impose a time depen-
 369 dent parametrization of s . We have thoroughly explored Kalman filter based approaches, but
 370 we ultimately prefer the method described in *Hines and Hetland* [2016] because of its rela-
 371 tive simplicity. Moreover, we believe the piecewise continuous representation of slip with re-
 372 spect to time to-be-is sufficiently general for the resolving power of these GPS data.

373 We estimate coseismic slip and afterslip with the same spatial and temporal discretiza-
 374 tion as in Section 3.1. Simultaneously, we estimate η_{eff} within six vertically stratified layers
 375 which have depths ranging from 15-30 km, 30-60 km, 60-90 km, 90-120 km, 120-150 km,

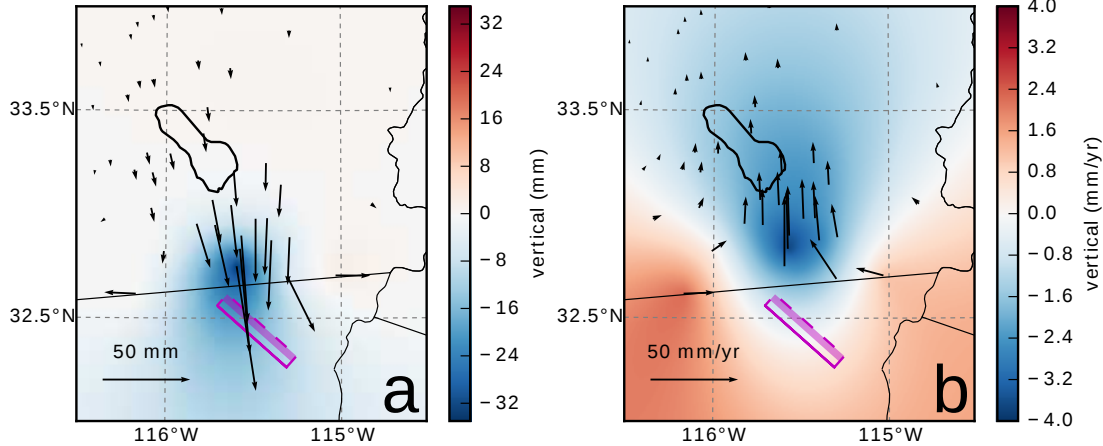


Figure 9. Displacements resulting from fault slip at lower crustal depths (a), and initial velocities resulting from subsequent relaxation of a viscoelastic lower crust (b). The fault segment dips 75° to the north-east and its surface projection is outlined in magenta. The highlighted area on the fault extends from 15 to 30 km depth and indicates where 1 meter of right-lateral slip was imposed. The elastic properties of the crust and mantle are the same as in Table 31, and η_{eff} is 10^{18} Pa s in the lower crust. Vertical displacements are interpolated between station locations.

from 150 km to the bottom of our numerical model domain at 800 km. We again restrict fault slip to occur between 0 and 15 km depth, which is done in order to help eliminate inevitable non-uniqueness in the inversion. It has long been recognized is well understood that fault slip at sufficiently great depths can produce surface deformation that is indistinguishable from viscoelastic relaxation, at least in two-dimensional earthquake models [Savage, 1990]. Additionally, we note that when simultaneously estimating both afterslip and viscosity in the lower crust, the inverse problem becomes particularly ill-posed. This ill-posedness is illustrated in Figure 9, which shows the displacements resulting from a meter of slip on a fault extending from 15 to 30 km depth and the initial velocity resulting from subsequent viscoelastic relaxation in the lower crust, which is given a viscosity of 10^{18} Pa s. In this demonstration, the viscoelastic relaxation is entirely driven by the fault slip in the lower crust. The horizontal displacements from fault slip are in the opposite direction as the displacements resulting from viscoelastic relaxation. This means that surface displacements resulting from afterslip at lower crustal depths can be cancelled out, at least partially, by a low viscosity lower crust. We eliminate this null space by allowing only one mechanism in the lower crust, which we choose to be viscoelastic relaxation. This is not to say that we do not believe deep afterslip to-be-is a possibility; rather, we restrict slip to seismogenic depths as a modeling necessity. Although, it has been noted that the pattern of vertical postseismic deformation following the El Mayor-Cucapah earthquake indicates that a significant amount of afterslip must be shallow [Rollins et al., 2015].

We must determine at which point the early postseismic approximation breaks down, which we will denote as t_{bd} . As noted, eq. (14) is valid for approximately as long as the rate of deformation resulting from viscoelastic relaxation is approximately constant. We can almost certainly assume that deformation at the most far-field stations, which are ~ 400 km away from the El Mayor-Cucapah epicenter, is the result of viscoelastic relaxation. The approximation should then be valid for as long as a linear trend adequately approximates the far-field deformation. Using this logic, it would appear that t_{bd} is about one year after the El Mayor-Cucapah earthquake. Another way to determine t_{bd} is to find the best fitting prediction of eq. (14) to observed deformation using increasing durations of the postseismic time series. t_{bd} should be the point when eq. (14) is no longer capable of describing the observed deformation without

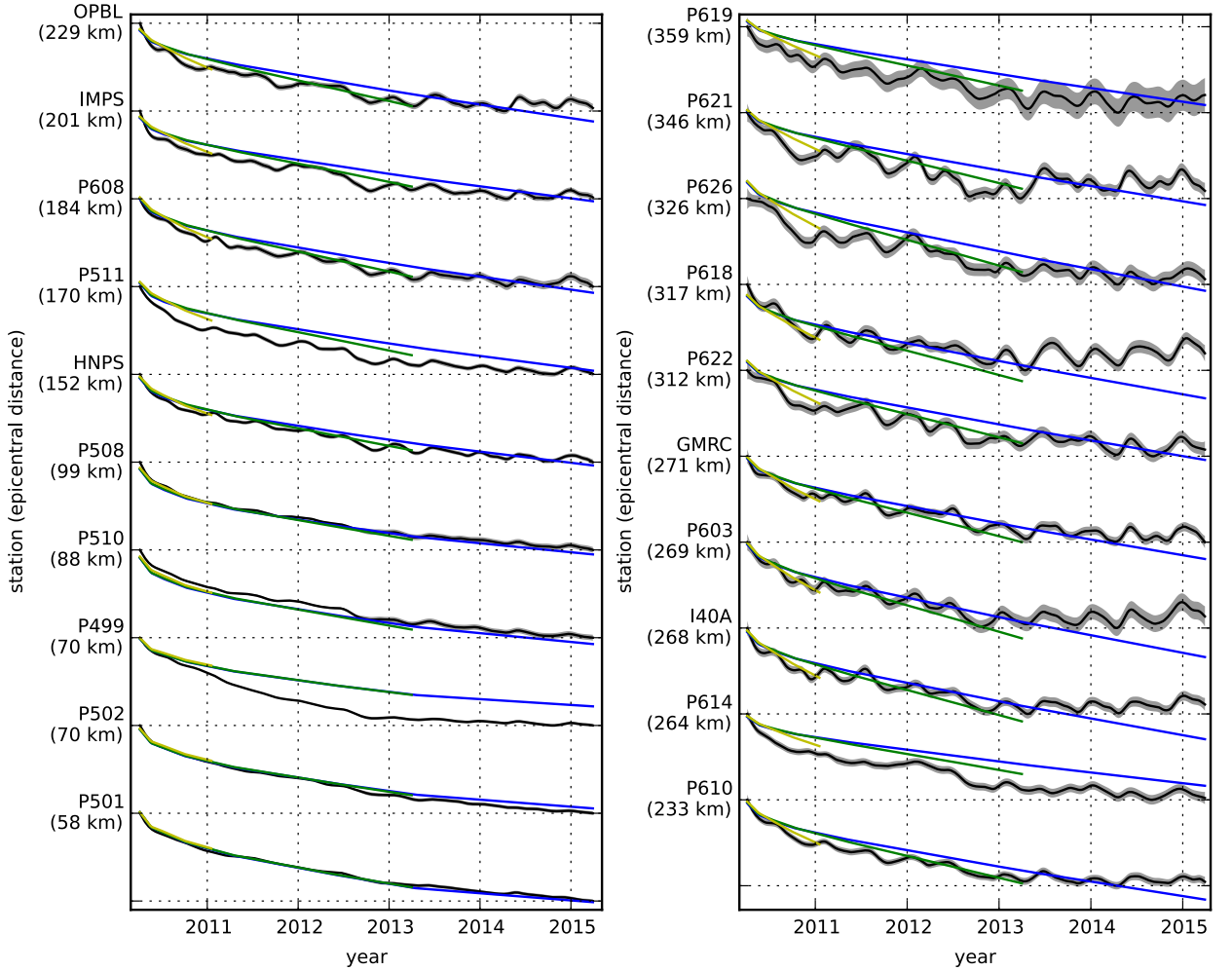


Figure 10. Observed postseismic displacements (black) and best fitting predictions of eq. (14) to 5.0 (blue), 3.0 (green), and 0.8 (yellow) years of the postseismic data.

incurring systematic misfits. When using eq. (14) to fit the entire five years of postseismic displacements, we see that the near-field displacements (e.g., station P501) are accurately predicted. When looking at displacements in the far-field (e.g., station P621), we see that eq. (14) overestimates the rate of deformation in the later postseismic period and underestimates the rate of deformation in the early period (Figure 10). Due to the low signal-to-noise ratios for far-field stations, it is difficult to determine at what point eq. (14) is no longer able to predict the observed displacements; however, we settle on $t_{bd} = 0.8$ years after the earthquake, while acknowledging that the choice is subjective. As noted in Hines and Hetland [2016], overestimating t_{bd} will result in a bias towards overestimating η_{eff} , while picking a t_{bd} which is too low will not necessarily result in a biased estimate of η_{eff} , although the uncertainties would be larger. We can then consider inferences of η_{eff} to be an upper bound on the viscosity needed to describe the far-field rate of deformation during the first 0.8 years of postseismic deformation.

We estimate coseismic slip, afterslip, and effective viscosities by solving

$$\min_{s, \eta_{eff}} \left(\left\| \frac{u_{pred}(s, \eta_{eff}) - u_{post}}{\sigma_{post}} \right\|_2^2 + \lambda_s \|s\|_2^2 + \lambda_\eta \|\nabla \eta_{eff}^{-1}\|_2^2 \right), \quad (15)$$

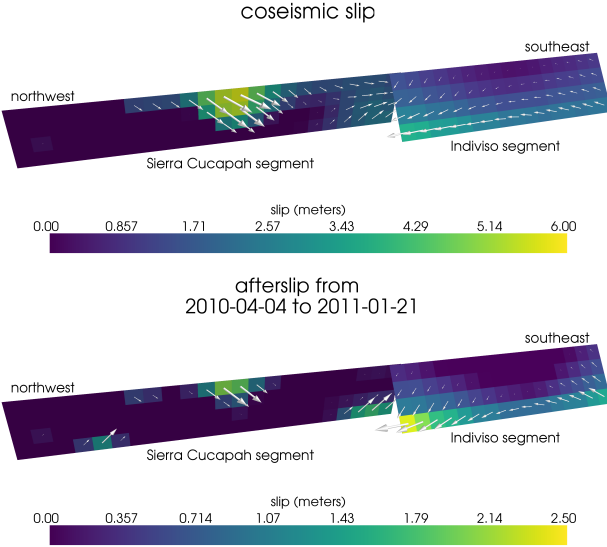
428 where u_{post} consists of the first 0.8 years of postseismic deformation and u_{pred} are the pre-
 429 dicted displacements from eq. (14). Due to inherent non-uniqueness, we have added zeroth-
 430 order Tikhonov regularization to estimates of s and second-order Tikhonov regularization to
 431 estimates of effective fluidity η_{eff}^{-1} . The degree to which we impose the regularization on slip
 432 and fluidity is controlled by the penalty parameters λ_s and λ_η , which are chosen with trade-
 433 off curves ([Figure S1](#)). Our goal [here](#) is to get a prior constraint on η_{eff} to minimize the amount
 434 of searching we have to do when describing the postseismic deformation over the full five years,
 435 which we do in Section 3.3. Estimates of s made here will not be used in Section 3.3, and
 436 so the motivation behind adding regularization to s is to ensure that the slip driving viscoelas-
 437 tic relaxation in eq. (14) is sensible.

438 Our [estimated effective viscosities, and corresponding fluidities, are shown in Figure 12](#).
 439 Although fluidity is rarely used in geophysical literature, eq. (13) is linear with respect to fluidity
 440 and so the fluidity indicates the amplitude of the viscoelastic signal coming from each layer.
 441 We also show the 95confidence intervals for estimated viscosities and fluidities but we note
 442 that the uncertainties tend to be underestimated due to the added regularization [[Aster et al., 2011](#)].
 443 A robust feature that we see is that the largest jump in fluidity is at 60 km depth, which is consistent
 444 with the range of lithosphere–asthenosphere boundary depths inferred by [Lekic et al. \[2011\]](#).
 445 This transitional depth is also consistent with the viscosity structure required to explain
 446 far-field postseismic deformation following the Hector Mine earthquake [[Freed et al., 2007](#)].
 447 We find that the viscosity below 60 km depth needs to be $\sim 10^{18}$ Pa s to describe the early
 448 rate of postseismic deformation at far-field stations while the lower crust and uppermost mantle
 449 need to be relatively stronger. The viscosity of the lower crust is the least well constrained as
 450 there is no evidence of relaxation in that layer, meaning that it is effectively elastic over the
 451 first 0.8 years after the earthquake.

452 Effective viscosities and associated fluidities inferred by fitting eq. (14) to the first 0.8
 453 years of postseismic displacements. 95confidence intervals, estimated from bootstrapping, are
 454 indicated by color fields.

455 Our initial estimate for coseismic slip and cumulative afterslip over the first 0.8 years
 456 after the El Mayor-Cucapah earthquake are shown in Figure 11. Similar to our elastic slip model
 457 from Section 3.1, a significant amount of right-lateral and normal coseismic slip is inferred
 458 to be on the Sierra Cucapah [fault segment](#). Our coseismic slip solution [on the Sierra Cucapah](#)
 459 [segment](#) is consistent with field studies [[Fletcher et al., 2014](#)] and the model from [Wei et al.](#)
 460 [[2011b](#)]. Our inferred slip on the Indiviso fault segment differs from [Wei et al. \[2011b\]](#) because
 461 the GPS data used in this study is not capable of resolving the spatial distribution of fault slip
 462 on that segment ([Figure S2](#)). The potency of inferred coseismic slip is 3.3×10^9 m³, which
 463 is also about the same as that inferred from Section 3.1. The present inference of afterslip on
 464 the Indiviso fault is significantly less than what was found in the Section 3.1 where we did
 465 not account for viscoelasticity. When fault slip is simultaneously estimated with viscosity, the
 466 potency of inferred afterslip over the first 0.8 years after the earthquake is 0.85×10^9 m³, com-
 467 pared to 3.5×10^9 m³ when we assume the crust and upper mantle are elastic. The signifi-
 468 cant amount of afterslip inferred on the Indiviso fault [in Section 3.1](#) seems to be compensat-
 469 ing for unmodeled viscoelastic relaxation[at depths greater than 60 km](#). The fact that there is
 470 still an appreciable amount of afterslip inferred on the Indiviso fault raises the question of whether
 471 it is compensating for viscoelastic relaxation that is more localized than what we allow for since
 472 we only estimate depth dependent variations in viscosity.

473 Our [estimated effective viscosities, and corresponding fluidities, are shown in Figure 12](#).
 474 Although fluidity is rarely used in geophysical literature, eq. (13) is linear with respect to fluidity
 475 and so the fluidity indicates the amplitude of the viscoelastic signal coming from each layer.
 476 We use bootstrapping to find the 95% confidence intervals for our estimated effective viscosities
 477 which are shown as shaded regions in Figure 12. It is important to remember that the presented
 478 effective viscosities were estimated with a smoothing regularization constraint and so the uncertainties
 479 are almost certainly underestimated [[Aster et al., 2011](#)]. Indeed, many viscosity profiles which
 480 are outside of the shown confidence intervals can just as adequately described the first 0.8 years



494 **Figure 11.** Coseismic slip and afterslip inferred by fitting eq. (14) to the first 0.8 years of postseismic
495 displacements.

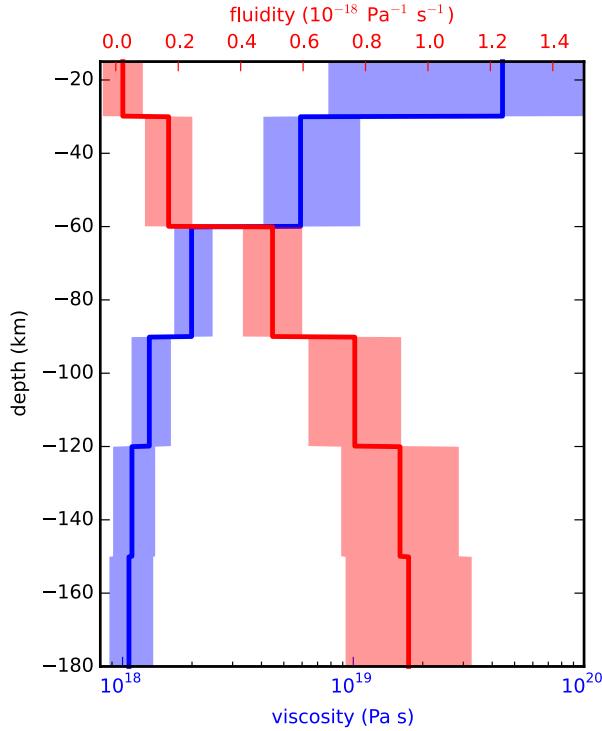
481 of postseismic deformation. Our solution in Figure 12 should be interpreted as the smoothest
482 effective viscosity profile which is capable of describing the data. This means that any sharp
483 viscosity transitions will be tapered out in the inversion, which we demonstrate with a synthetic
484 test in Figure S2. Nonetheless, a robust feature that we see with a variety of choices for λ_s ,
485 λ_u , and t_{bd} is that the largest jump in fluidity is at 60 km depth, which is consistent with the
486 range of lithosphere-asthenosphere boundary depths inferred by Lekic *et al.* [2011]. This transitional
487 depth is also consistent with the the viscosity structure required to explain far-field postseismic
488 deformation following the Hector Mine earthquake [Freed *et al.*, 2007]. We find that the viscosity
489 below 60 km depth needs to be $\sim 1 \times 10^{18}$ Pa s to describe the early rate of postseismic deformation
490 at far-field stations while the lower crust and uppermost mantle need to be relatively stronger.
491 The viscosity of the lower crust has the largest uncertainties because there is no evidence of
492 relaxation in that layer, meaning that it is effectively elastic over the first 0.8 years after the
493 earthquake.

499 3.3 Full Postseismic Inversion

500 In the previous section, we used the inverse method from Hines and Hetland [2016] to
501 constrain the effective viscosity structure required to explain the first 0.8 years of postseismic
502 deformation. In this section, we use these effective viscosities as a prior constraint when search-
503 ing for models which are capable of describing the available five years of postseismic data,
504 where our forward problem is now eq. (11) rather than the approximation given by eq. (14).
505 We perform a series of fault slip inversions assuming a variety of rheologies for the lower crust
506 and upper mantle which are consistent with our findings from Section 3.2. We appraise each
507 model using the mean chi-squared value,

$$\chi^2 = \frac{1}{N} \left\| \frac{u_{\text{pred}} - u_{\text{obs}}}{\sigma_{\text{obs}}} \frac{u_{\text{pred}} - u_{\text{post}}}{\sigma_{\text{post}}} \right\|_2^2, \quad (16)$$

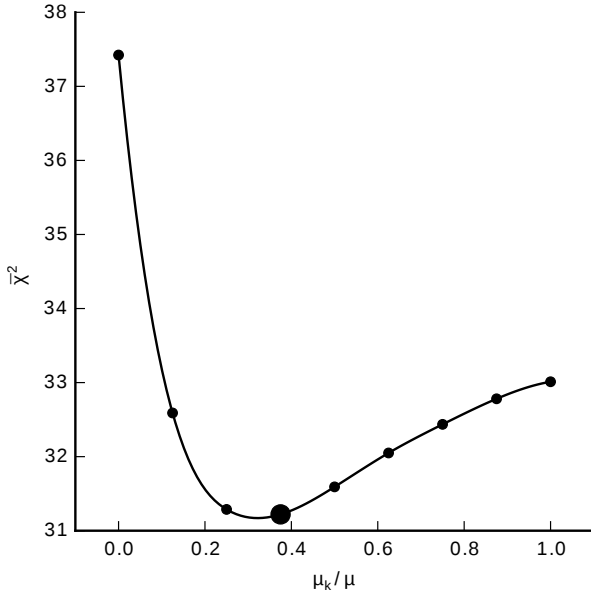
508 where N is the number of observations.



496 **Figure 12.** Effective viscosities and associated fluidities inferred by fitting eq. (14) to the first 0.8 years of
 497 postseismic displacements. 95% confidence intervals, estimated from bootstrapping, are indicated by shaded
 498 regions.

509 We first assume that the crust and mantle can be described with a Maxwell rheology,
 510 and we set the steady-state viscosity, η_M , equal to our inference of η_{eff} . We compute f and
 511 g from eq. (11) using Pylith, and we use the same spatial and temporal discretization of s as
 512 in Sections 3.1 and 3.2. We estimate s using linear least squares and find a misfit of $\bar{\chi}^2 =$
 513 37.4. For comparison, $\bar{\chi}^2 = 35.3$ for the elastic model from Section 3.1. The Maxwell vis-
 514 coelastic model has a larger misfit because it tends to overestimate the rate of deformation af-
 515 ter about three years (Figure ??7). Since our initial estimates of η_{eff} may be biased towards
 516 overestimating viscosities, we have also performed the slip inversion where we use uniformly
 517 lower viscosities in the crust and mantle. However, however, decreasing the viscosity only in-
 518 creases the misfit. Although, the viscosities used here are consistent with the successful Maxwell
 519 viscoelastic models found by Rollins *et al.* [2015] and Spinler *et al.* [2015], which had man-
 520 tle viscosities on the order of 10^{18} Pa s and relatively higher lower crustal viscosities, we find
 521 that such a model is incapable of describing the entire postseismic time series. Pollitz *et al.*
 522 [2001] similarly recognized this deficiency in a Maxwell rheology, which then motivated their
 523 exploration of a Burgers rheology upper mantle [Pollitz, 2003].

524 Instead of exploring a Burgers rheology mantle, which introduces two new parameters
 525 that need to be estimated, the transient viscosity, η_K , and transient shear modulus, μ_K , we first
 526 consider a Zener rheology for the mantle, which only introduces one additional unknown
 527 model parameter, μ_K . We assume that the lower crust still has a Maxwell rheology. The steady-
 528 state viscosity in the crust and the transient viscosity in the mantle are set equal to the inferred
 529 effective viscosities. We then estimate the ratio of shear moduli, $\frac{\mu_K}{\mu}$. We compute nine dif-
 530 ferent sets of Green's functions, f and g , where we assume values of $\frac{\mu_K}{\mu}$ ranging from 0 to
 531 1. The former being a degenerate case where the Zener model reduces to the above Maxwell
 532 model. We estimate coseismic slip and afterslip for each realization of $\frac{\mu_K}{\mu}$. The We find that



539 **Figure 13.** Mean chi-squared value for the best fitting slip model as a function of the transient shear mod-
 540 ulus relative to the elastic shear modulus in a Zener rheology upper mantle. Large dot indicates our preferred
 541 ratio.

533 a shear moduli ratio that of 0.375 yields the best prediction to the observed postseismic dis-
 534 placements is found to be 0.375 which produces with a misfit of $\bar{\chi}^2 = 31.2$ (Figure 13). The
 535 improvement in the Zener model over the Maxwell model can be clearly seen in the fit to the
 536 far-field data (Figure ??). The 7 where the Zener model does a significantly better job at ex-
 537 plaining the transient rate of far-field deformation throughout the five years - considered in this
 538 study. The rheologic parameters for our preferred Zener model are summarized in Table 1.

542 Observed postseismic displacements (black). Predicted postseismic displacements for the
 543 best fitting slip model when assuming a Maxwell viscoelastic lower crust and upper mantle
 544 (blue). Predicted postseismic displacements for the best fitting slip model when assuming a
 545 Maxwell viscoelastic lower crust and a Zener viscoelastic upper mantle (green). The effective
 546 viscosities are the same for both models and are shown in Figure 12.

547 Because we are able to adequately describe the available five years of postseismic de-
 548 formation with a Zener model, we do not find it necessary to explore the parameter space for
 549 a more complicated Burgers rheology. However, since the Zener model is a Burgers model with
 550 an infinite steady-state viscosity, we can conclude that any Burgers rheology that has a trans-
 551 sient viscosity consistent with that found in Section 3.2 and a steady-state viscosity $\gtrsim 10^{20}$
 552 Pa s, which is effectively infinite on the time scale of five years, would also be able to sat-
 553 isfactorily describe the observable postseismic deformation.

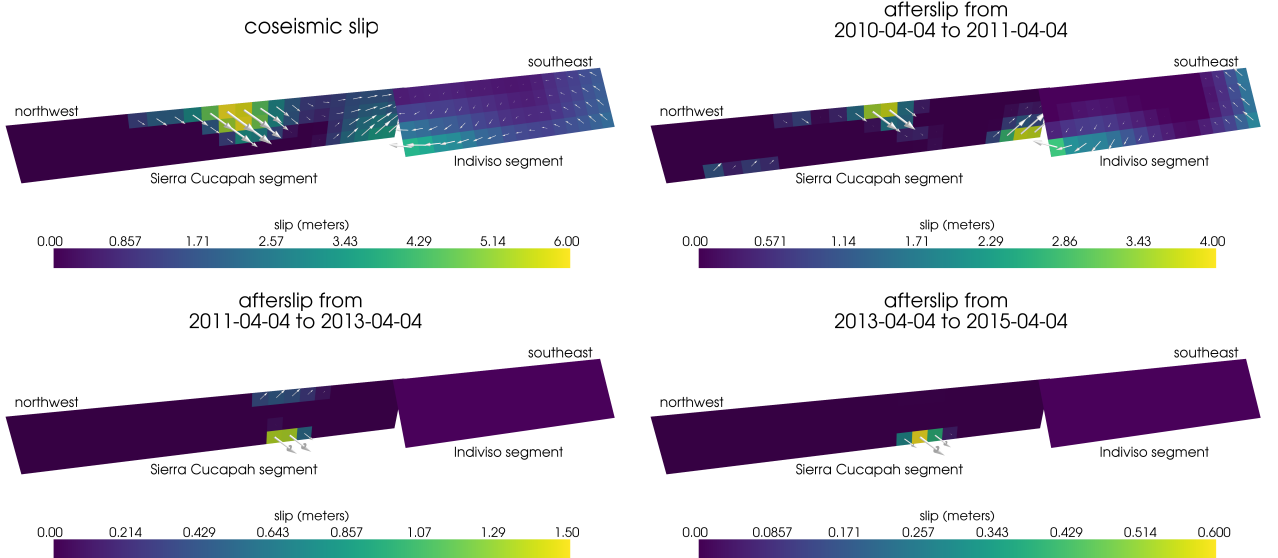
554 The regularized inference of coseismic slip and afterslip for our preferred Zener model
 555 is shown in Figure 14. The inferred coseismic potency is $3.0 \times 10^9 \text{ m}^3$, equivalent to a Mw7.26
 556 earthquake, and Mw=7.26 earthquake, where most of the slip is shallow and on the Sierra Cu-
 557 capah fault segment. The potency of five years of afterslip is $1.1 \times 10^9 \text{ m}^3$. Most of the af-
 558terslip in our preferred model occurs within the first year after the earthquake and coincides
 559 with the location of our inferred coseismic slip. Inferred afterslip within the first year is ac-
 560 counting for the most rapid near-field transient deformation (Figure S3). After one year, af-
 561terslip is inferred to be deeper down on the Sierra Cucaph segment, which is describing much
 562 of the . The sustained near-field postseismic deformation is being explained by this continued
 563 afterslip as well as viscoelastic relaxation in the lower crust. We emphasize, that the GPS sta-

tion closest to where we infer afterslip, P496, is still about 30 km away, which is too far for us to conclusively ~~argue for sustained localized deformation rather than shallow distributed deformation discern deep afterslip from viscoelastic relaxation in the lower crust~~. The deep afterslip inferred after one year could potentially be ~~describing deformation resulting from lower crustal flow compensating for an overestimated lower crustal viscosity~~. To test this, we have modified our preferred model by decreasing the lower crustal viscosity from 5.91×10^{19} Pa s to 1×10^{19} Pa s, which is still consistent with our viscosity inference from Section 3.2, and ~~we~~ inverted for fault slip. We find that a model with a weaker lower crust adequately describes the postseismic displacements without any afterslip after one year, while still requiring about the same amount of afterslip over the first year. We do believe that the early ~~shallow~~ afterslip on the Sierra Cucapah segment is a robust feature in our preferred model, while we are not confident in our inference of later deep afterslip.

~~the~~ ~~The~~ postseismic displacements predicted by our preferred Zener model are shown in Figures 4, 5 and ?? ~~. Overall, the trends in the near-field and far-field transient deformation are accurately described. In particular, the trends in far-field deformation are much better described by our preferred Zener model than either an elastic model or a model with a Maxwell viscoelastic mantle (Figure ??).~~ There are a few areas where we have notable misfit. Most of our misfit is for the near-field stations in the Imperial Valley, and we attribute this misfit to our relatively simple fault geometry, which does not account for potential 7. The largest misfit occur within the Imperial Valley where there does not appear to be any systematic trend in the residuals. This suggests that the large errors are due to localized processes such as fault slip in the Imperial Valley triggered by the El Mayor-Cucapah earthquake [Wei *et al.*, 2011a, 2015]. ~~In particular, we are unable to model the sustained, rapid rate of deformation at station P496, which suggests that this station could be influenced by a more localized deformation mechanism than is considered in this study~~ We do not see any pattern in the residuals that would suggest a laterally heterogeneous viscosity structure, which has been explored by Pollitz *et al.* [2012] and Rollins *et al.* [2015]. We do notice regional scale seasonal oscillations in the lateral and vertical components of the residuals with an amplitude of 1-2 millimeters. This is the result of our method for data processing which is not able to completely remove the seasonal signal in the GPS data, which was discussed in Section 2. Additionally, we see systematic misfit in the later postseismic period west of the Landers and Hector Mine earthquakes, which may be the result of unmodeled postseismic deformation resulting from following those earthquakes. Lastly, there are clear discrepancies between the observed and predicted vertical deformation displacements following the first year after the El ~~Mayor-Cucapah~~ ~~Major-Cucapah~~ earthquake. We observe a broad uplift throughout Southern California, which is inconsistent with any postseismic model.

603 4 Discussion

604 It has long been recognized that deep afterslip and viscoelastic relaxation following an
 605 upper crustal earthquake can result in similar horizontal ground deformation at the surface [e.g.
 606 Savage, 1990; Pollitz *et al.*, 2001; Hearn, 2003; Feigl and Thatcher, 2006]. The similarity of
 607 the horizontal postseismic deformation results in a non-uniqueness in inferences of afterslip
 608 or viscoelastic relaxation. ~~In contrast, the~~ ~~The~~ spatial pattern of vertical postseismic deformation
 609 has been proposed to be a discriminant between deep afterslip and viscoelastic relaxation
 610 [e.g. Pollitz *et al.*, 2001; Hearn, 2003]. It is, however, important to note that patterns of ver-
 611 tical deformation are very sensitive to the depth-dependence of viscosity below the upper crust
 612 [Yang and Toksöz, 1981; Hetland and Zhang, 2014]. The similarity between deformation re-
 613 sulting from deep afterslip and viscoelastic relaxation of coseismic stresses is different from
 614 the ill-posedness described in Section 3.2. In our method, any inferred afterslip will also me-
 615 chanically drive additional viscoelastic relaxation. The horizontal deformation resulting from
 616 deep afterslip will generally be in the opposite direction as horizontal deformation resulting
 617 from viscoelastic relaxation of subsequent stresses in the lower crust (Figure 9). As a result,
 618 there is a trade-off between inferences of deep afterslip and lower crustal viscosity. In our syn-
 619 synthetic tests in Hines and Hetland [2016], we have found that inverting surface deformation for



599 **Figure 14.** Inferred coseismic slip and afterslip when assuming for our preferred model, which has a
600 Maxwell rheology in the lower crust and a Zener rheology in the upper mantle. The transient viscosity, η_K , in
601 the mantle and steady-state viscosity, η_M , in the crust are set equal to the effective viscosities from Figure 12.
602 We set use $\frac{\mu_K}{\mu} = 0.375$ in the upper mantle.

620 afterslip and viscosity within the same depth interval tends to result in overestimated afterslip
621 and an underestimated viscosity.

622 Most postseismic studies assume Maxwell viscoelasticity in the lower crust and upper
623 mantle [e.g. Nur and Mavko, 1974; Pollitz et al., 2000; Hetland, 2003; Freed et al., 2006; John-
624 son et al., 2009; Hearn et al., 2009], which is the simplest viscoelastic rheologic model. In South-
625 ern California, postseismic studies following the Landers [Pollitz et al., 2000], Hector Mine
626 [Pollitz et al., 2001], and El Mayor-Cucapah earthquake [Spinler et al., 2015; Rollins et al., 2015],
627 have assumed Maxwell viscoelasticity in the lower crust and upper mantle and have inferred
628 upper mantle viscosities on the order of 10^{17} to 10^{18} Pa s and lower crust viscosities $\gtrsim 10^{19}$
629 Pa s. These postseismic studies are consistent with Kaufmann and Amelung [2000] and Cav-
630 alié et al. [2007], who found that an upper mantle viscosity of 10^{18} Pa s and a crustal viscosity
631 $\gtrsim 10^{20}$ Pa s are necessary to describe subsidence resulting from changes in loading from
632 Lake Mead. This isostatic adjustment is a process with similar spatial and temporal scales as
633 postseismic deformation, and thus the inferred viscosities of these two types of studies would
634 likely agree. While these studies found viscosities that are consistent with our effective vis-
635 cosities from Section 3.2, they are inconsistent with viscosity estimates made from geophys-
636 ical processes that occur over longer time scales. For example, Lundgren et al. [2009] found
637 that lower crust and upper mantle viscosities on the order of 10^{21} and 10^{19} Pa s, respectively,
638 are needed to describe interseismic deformation along the Southern San Andreas fault zone
639 in the Salton Sea region. An even higher mantle viscosity, on the order of 10^{20} Pa s, is re-
640 quired to describe isostatic adjustment resulting from the draining of Lake Bonneville, which
641 occurs on the time scales of 10^4 years [Crittenden, 1967; Bills and May, 1987].

642 An additional deficiency with the Maxwell rheology is that it predicts a steady decay
643 in the rate of postseismic deformation over time, which fails to describe the commonly ob-
644 served rapid, early transience followed by a relatively steady rate of postseismic deformation.
645 One could explain the early transient postseismic deformation with fault creep and the later
646 phase with relaxation in a Maxwell viscoelastic lower crust and upper mantle [e.g. Hearn et al.,

647 2009; *Johnson et al.*, 2009]. However, postseismic deformation at distances greater than ~ 200
 648 km from the El Mayor-Cucapah epicenter can only be attributed to viscoelastic relaxation [Freed et al.,
 649 we have demonstrated that the far-field deformation cannot be explained with a Maxwell rheo-
 650 logy (Figure ??7).

651 We found that a Zener rheology in the upper mantle with a transient viscosity of $\sim 10^{18}$
 652 Pa s does a noticeably better job at predicting far-field postseismic deformation. A general-
 653 ization of the Zener viscoelastic model, schematically represented as several Kelvin elements
 654 connected in series, is commonly used to describe seismic attenuation [Liu et al., 1976]. The
 655 highest viscosity needed to describe seismic attenuation is on the order of 10^{16} Pa s [Yuen and
 656 Peltier, 1982] which has a characteristic relaxation time on the order of days. Even though
 657 our inferred transient viscosity is orders of magnitude larger than that required for seismic at-
 658 tenuation models, the two models are not incompatible. Rather, the delayed elasticity in seis-
 659 mic attenuation models occurs on such short time scales that it can be considered part of the
 660 instantaneous elastic phase of deformation associated with the preferred Zener model in this
 661 study.

662 Of course, ~~it has long been recognized that~~ a Zener rheology provides an incomplete ~~descriptions~~
 663 ~~description~~ of the asthenosphere, ~~as because~~ it does not have the fluid-like behavior required
 664 to explain isostatic rebound or convection in the mantle [O'Connell, 1971]. Yuen and Peltier
 665 [1982] proposed a Burgers rheology with a low transient viscosity ($\eta_K \approx 10^{16}$ Pa s) and high
 666 steady-state viscosity ($\eta_M \approx 10^{21}$ Pa s) to describe both seismic attenuation and long term
 667 geologic processes. The justification of a Burger's rheology mantle is further supported by lab-
 668 oratory experiments on olivine [Chopra, 1997]. Pollitz [2003] sought to describe postseismic
 669 deformation following Hector Mine with a Burgers rheology mantle and they found a best fit-
 670 ting transient viscosity of 1.6×10^{17} Pa s and steady-state viscosity of 4.6×10^{18} Pa s. While
 671 the Burgers rheology was introduced as a means of bridging the gap between relaxation ob-
 672 served in long and short term geophysical processes, the inferred steady state viscosity from
 673 Pollitz [2003] is still inconsistent with the Maxwell viscosities inferred from studies on the earth-
 674 quake cycle and Lake Bonneville. The transient viscosity inferred by Pollitz [2003] is constrained
 675 by the earliest phase of postseismic deformation following the Hector Mine earthquake. While
 676 Pollitz [2003] ruled out deep afterslip as an alternative mechanism based on inconsistent ver-
 677 tical deformation, it is still possible to successfully describe all components of early postseis-
 678 mic deformation following the Hector Mine earthquake with afterslip at seismogenic depths
 679 [Jacobs et al., 2002]. It is then possible that the preferred rheologic model from Pollitz [2003]
 680 was biased towards inferring a particularly low transient viscosity by neglecting to account for
 681 afterslip. This is in contrast to the present study, where we have inferred a viscosity structure
 682 simultaneously with afterslip. We also argue that a transient rheology is necessary to explain
 683 postseismic deformation; however, our preferred transient viscosity of $\sim 10^{18}$ Pa s in the up-
 684 per mantle is an order of magnitude larger than the transient viscosity found by Pollitz [2003].
 685 ~~The transient viscosity inferred here is consistent with the results of Pollitz [2015], who reanalyzed~~
 686 ~~postseismic data following the Landers and Hector Mine earthquake allowing the first few months~~
 687 ~~of transient deformation to be described by afterslip.~~ Since a Zener model is able to describe
 688 the available postseismic deformation following the El Mayor-Cucapah earthquake, any Burg-
 689 ers rheology with a steady-state viscosity that is $\gtrsim 10^{20}$ Pa s, effectively infinite over five years,
 690 would also be able to describe the postseismic deformation. Such a Burgers model might then
 691 be consistent with the steady-state viscosities necessary for lake loading, interseismic defor-
 692 mation, and mantle dynamics.

693 5 Conclusion

694 We have extracted a ~~filtered-and~~-smoothed estimate of postseismic deformation follow-
 695 ing the El Mayor-Cucapah earthquake from GPS displacement time series. Our estimated post-
 696 seismic deformation reveals far-field (epicentral distances ~~beyond~~ ~ 200 $\gtrsim 200$ km) transient
 697 deformation which is ~~largely~~-undetectable after about three years. Near-field deformation ex-
 698 hibits transience that decays to a sustained, elevated rate after about one or two years. We found

699 that near-field transient deformation can be explained with shallow afterslip, ~~and the~~. The sus-
 700 tained rate of near-field deformation can ~~either~~ be explained with ~~continued afterslip or~~ vis-
 701 coelastic relaxation in the lower crust and possibly continued afterslip. Far-field transient de-
 702 formation can be more definitively ascribed to viscoelastic relaxation at depths greater than
 703 ~60 km. Beneath that depth, a transient viscosity of $\sim 10^{18}$ $\sim 1 \times 10^{18}$ Pa s is required to de-
 704 scribe the rate of far-field deformation throughout the five years considered in this study. By
 705 describing the available postseismic deformation with a transient rheology in the mantle, our
 706 preferred model does not conflict with the generally higher steady-state viscosities inferred from
 707 geophysical processes occurring over longer time scales.

708 Acknowledgements

709 We thank Andy Freed for an illuminating discussion on the data used in this study. We
 710 thank Fred Pollitz and an anonymous reviewer for comments that improved this manuscript.
 711 We also thank the editor, Martha Savage. This material is based on EarthScope Plate Bound-
 712 ary Observatory data services provided by UNAVCO through the GAGE Facility with support
 713 from the National Science Foundation (NSF) and National Aeronautics and Space Adminis-
 714 tration (NASA) under NSF Cooperative Agreement No. EAR-1261833. The data used in this
 715 study can be found at www.unavco.org. This material is based upon work supported by the
 716 National Science Foundation under Grant Numbers EAR 1045372 and EAR 1245263.

717 References

- 718 Agaard, B. T., M. G. Knepley, and C. A. Williams (2013), A domain decomposition
 719 approach to implementing fault slip in finite-element models of quasi-static and dy-
 720 namic crustal deformation, *Journal of Geophysical Research: Solid Earth*, 118, doi:
 721 10.1002/jgrb.50217.
- 722 Argus, D. F., M. B. Heflin, G. Peltzer, F. Crampé, and F. H. Webb (2005), Interseismic
 723 strain accumulation and anthropogenic motion in metropolitan Los Angeles, *Journal of*
 724 *Geophysical Research: Solid Earth*, 110(B04401), 1–26, doi:10.1029/2003JB002934.
- 725 Aster, R. C., B. Borchers, and C. H. Thurber (2011), Parameter Estimation and Inverse
 726 Problems, vol. 90, Academic Press.
- 727 Bawden, G. W., W. Thatcher, R. S. Stein, K. W. Hudnut, and G. Peltzer (2001), Tectonic
 728 contraction across Los Angeles after removal of groundwater pumping effects., *Nature*,
 729 412(August), 812–815, doi:10.1038/35090558.
- 730 Bills, B. G., and G. M. May (1987), Lake Bonneville: Constraints on Lithospheric Thick-
 731 ness and Upper Mantle Viscosity From Isostatic Warping of Bonneville, Provo, and
 732 Gilbert Stage Shorelines, *Journal of Geophysical Research-Solid Earth and Planets*,
 733 92(B11), 11, 493–11,50811493–11508, doi:10.1029/JB092iB11p11493.
- 734 Çakir, Z., S. Ergintav, H. Özener, U. Dogan, A. M. Akoglu, M. Meghraoui, and
 735 R. Reilinger (2012), Onset of aseismic creep on major strike-slip faults, *Geology*,
 736 40(12), 1115–1118, doi:10.1130/G33522.1.
- 737 Cavalié, O., M. P. Doin, C. Lasserre, and P. Briole (2007), Ground motion measurement in
 738 the Lake Mead area, Nevada, by differential synthetic aperture radar interferometry time
 739 series analysis: Probing the lithosphere rheological structure, *Journal of Geophysical*
 740 *Research: Solid Earth*, 112(B03403), 1–18, doi:10.1029/2006JB004344.
- 741 Cetin, E., Z. Çakir, M. Meghraoui, S. Ergintav, and A. M. Akoglu (2014), Extent and
 742 distribution of aseismic slip on the İsmetpaşa segment of the North Anatolian Fault
 743 (Turkey) from Persistent Scatterer InSAR, *Geochemistry, Geophysics, Geosystems*, 15,
 744 doi:10.1002/2014GC005307.
- 745 Chopra, P. N. (1997), High-temperature transient creep in olivine rocks, *Tectonophysics*,
 746 279, 93–111, doi:10.1016/S0040-1951(97)00134-0.
- 747 Crittenden, M. (1967), Viscosity and Finite Strength of the Mantle as Determined from
 748 Water and Ice ~~Loads~~*Loads, *Geophysical Journal of the Royal Astronomical Society*,

- 749 pp.-261–279, doi:10.1111/j.1365-246X.1967.tb06243.x.
- 750 Davis, J. L., B. P. Wernicke, and M. E. Tamisiea (2012), On seasonal signals in geodetic
751 time series, *Journal of Geophysical Research: Solid Earth*, [117\(B01403\)](#), 1–10, doi:
752 10.1029/2011JB008690.
- 753 Feigl, K. L., and W. Thatcher (2006), Geodetic observations of post-seismic transients in
754 the context of the earthquake deformation cycle, *Comptes Rendus - Geoscience*, [338](#),
755 1012–1028, doi:10.1016/j.crte.2006.06.006.
- 756 Fletcher, J. M., O. J. Teran, T. K. Rockwell, M. E. Osokin, K. W. Hudnut, K. J. Mueller,
757 R. M. Spelz, S. O. Akciz, E. Masana, G. Faneros, E. J. Fielding, S. Leprince, A. E.
758 Morelan, J. Stock, D. K. Lynch, A. J. Elliott, P. Gold, J. Liu-Zeng, A. González-
759 Ortega, A. Hinojosa-Corona, and J. González-García (2014), Assembly of a large
760 earthquake from a complex fault system: Surface rupture kinematics of the 4 April
761 2010 El Mayor-Cucapah (Mexico) Mw 7.2 earthquake, *Geosphere*, [10\(4\)](#), 797–827,
762 doi:10.1130/GES00933.1.
- 763 Freed, A. M., R. Bürgmann, E. Calais, J. Freymueller, and S. Hreinsdóttir (2006), Impli-
764 cations of deformation following the 2002 Denali, Alaska, earthquake for postseismic
765 relaxation processes and lithospheric rheology, *Journal of Geophysical Research: Solid
766 Earth*, [111\(B01401\)](#), 1–23, doi:10.1029/2005JB003894.
- 767 Freed, A. M., R. Bürgmann, and T. Herring (2007), Far-reaching transient motions after
768 Mojave earthquakes require broad mantle flow beneath a strong crust, *Geophysical
769 Research Letters*, [34\(L19302\)](#), 1–5, doi:10.1029/2007GL030959.
- 770 Gonzalez-Ortega, A., Y. Fialko, D. Sandwell, F. A. Nava-pichardo, J. Fletcher,
771 J. Gonzalez-garcia, B. Lipovsky, M. Floyd, and G. Funning (2014), El Mayor-Cucapah
772 (Mw7.2) earthquake: early near-field postseismic deformation from InSar and GPS
773 observations, *Journal of Geophysical Research: Solid Earth*, [119](#), 1482–1497, doi:
774 10.1002/2013JB010193.
- 775 Hauksson, E., J. Stock, K. Hutton, W. Yang, J. A. Vidal-Villegas, and H. Kanamori
776 (2011), The 2010 Mw 7.2 El mayor-cucapah earthquake sequence, Baja California,
777 Mexico and Southernmost California, USA: Active seismotectonics along the Mexican
778 pacific margin, *Pure and Applied Geophysics*, [168](#), 1255–1277, doi:10.1007/s00024-010-
779 0209-7.
- 780 Hearn, E. H. (2003), What can GPS data tell us about the dynamics of post-seismic defor-
781 mation?, [\(2003\)Geophysical Journal International](#), [115](#), 753–777, doi:10.1111/j.1365-
782 246X.2003.02030.x.
- 783 Hearn, E. H., S. McClusky, S. Ergintav, and R. E. Reilinger (2009), Izmit earthquake
784 postseismic deformation and dynamics of the North Anatolian Fault Zone, *Jour-
785 nal of Geophysical Research: Solid Earth*, [114\(August 2008B08405\)](#), 1–21, doi:
786 10.1029/2008JB006026.
- 787 Hetland, E. A. (2003), Postseismic relaxation across the Central Nevada Seismic Belt,
788 *Journal of Geophysical Research*, [108\(Figure 2B8\)](#), 1–13, doi:10.1029/2002JB002257.
- 789 Hetland, E. A., and G. Zhang (2014), Effect of shear zones on post-seismic deformation
790 with application to the 1997 Mw 7.6 manyi earthquake, *Geophysical Journal Interna-
791 tional*, [198–259–269206\(2\)](#), 1–11, doi:10.1093/gji/ggu127.
- 792 Hines, T. T., and E. A. Hetland (2013), Bias in estimates of lithosphere viscosity from
793 interseismic deformation, *Geophysical Research Letters*, [40\(16\)](#), 4260–4265, doi:
794 10.1002/grl.50839.
- 795 Hines, T. T., and E. A. Hetland (2016), Rapid and simultaneous estimation of fault slip
796 and heterogeneous lithospheric viscosity from post-seismic deformation, *Geophysical
797 Journal International*, [204\(1\)](#), 569–582, doi:10.1093/gji/ggv477.
- 798 Jacobs, A., D. Sandwell, Y. Fialko, and L. Sichoux (2002), The 1999 (Mw7.1) Hector
799 Mine, California, Earthquake: Near-Field Postseismic Deformation from ERS Interfer-
800 ometry, *Bulletin of the Seismological Society of America*, [92\(May\)92\(4\)](#), 1433–1442.
- 801 Johnson, K. M., and P. Segall (2004), Viscoelastic earthquake cycle models with deep
802 stress-driven creep along the San Andreas fault system, *Journal of Geophysical Re-*

- 803 *searchB: Solid Earth*, [109\(B10403\)](#), 1–19, doi:10.1029/2004JB003096.
- 804 Johnson, K. M., R. Bürgmann, and J. T. Freymueller (2009), Coupled afterslip and vis-
805 coelastic flow following the 2002 Denali Fault, Alaska earthquake, *Geophysical Journal
International*, [176](#)(3), 670–682, doi:10.1111/j.1365-246X.2008.04029.x.
- 806 Jónsson, S., P. Segall, R. Pedersen, and G. Bjornsson (2003), Post-earthquake ground
807 movements correlated to pore-pressure transients, *Nature*, [424](#)(July), 179–183, doi:
808 10.1038/nature01758.1.
- 809 Kaufmann, G., and F. Amelung (2000), Reservoir-induced deformation and continental
810 rheology in vicinity of Lake Mead, Nevada, *Journal of Geophysical Research*, [105](#)(B7),
811 16,341, doi:10.1029/2000JB900079.
- 812 Kroll, K. A., E. S. Cochran, K. B. Richards-Dinger, and D. F. Sumy (2013), Aftershocks
813 of the 2010 Mw 7.2 El Mayor-Cucapah earthquake reveal complex faulting in the Yuha
814 Desert, California, *Journal of Geophysical Research: Solid Earth*, [118](#)(October), 6146–
815 6164, doi:10.1002/2013JB010529.
- 816 Lekic, V., S. W. French, and K. M. Fischer (2011), Lithospheric Thinning Beneath Rifted
817 Regions of Southern California, *Science*, [334](#)(November), 783–787.
- 818 Liu, H.-P., D. L. Anderson, and H. Kanamori (1976), Velocity dispersion due to anelas-
819 ticity; implications for seismology and mantle composition, *Geophysical Journal of
the Royal Astronomical Society*, *Geophysical Journal International*, [47](#), 41–58, doi:
820 10.1111/j.1365-246X.1976.tb01261.x.
- 821 Lundgren, P., E. A. Hetland, Z. Liu, and E. J. Fielding (2009), Southern San Andreas-San
822 Jacinto fault system slip rates estimated from earthquake cycle models constrained by
823 GPS and interferometric synthetic aperture radar observations, *Journal of Geophysical
Research: Solid Earth*, [114](#)(B02403), 1–18, doi:10.1029/2008JB005996.
- 824 McGuire, J. J., and P. Segall (2003), Imaging of aseismic fault slip transients recorded
825 by dense geodetic networks, *Geophysical Journal International*, [155](#), 778–788, doi:
826 10.1111/j.1365-246X.2003.02022.x.
- 827 Meade, B. J., and B. H. Hager (2005), Block models of crustal motion in southern Cal-
828 ifornia constrained by GPS measurements, *Journal of Geophysical ResearchB: Solid
Earth*, [110](#)(B03403), 1–19, doi:10.1029/2004JB003209.
- 829 Murray, J. R., and P. Segall (2005), Spatiotemporal evolution of a transient slip event on
830 the San Andreas fault near Parkfield, California, *Journal of Geophysical Research: Solid
Earth*, [110](#)(B09407), 1–12, doi:10.1029/2005JB003651.
- 831 Nur, A., and G. Mavko (1974), Postseismic viscoelastic rebound, *Science*, [183](#)(4121),
832 204–206, doi:10.1038/098448b0.
- 833 O'Connell, R. J. (1971), Rheology of the Mantle, *EOS, Transactions, American Geophys-
ical Union*, [52](#), 140–142.
- 834 Oskin, M. E., J. R. Arrowsmith, A. Hinojosa Corona, A. J. Elliott, J. M. Fletcher, E. J.
835 Fielding, P. O. Gold, J. J. Gonzalez Garcia, K. W. Hudnut, J. Liu-Zeng, and O. J. Teran
836 (2012), Near-field deformation from the El Mayor-Cucapah earthquake revealed by
837 differential LIDAR, *Science*, [335](#), 702–705, doi:10.1126/science.1213778.
- 838 Pollitz, F., C. Wicks, and W. Thatcher (2001), Mantle Flow Beneath a Continental Strike-
839 Slip Fault: Postseismic Deformation After the 1999 Hector Mine Earthquake, *Science*,
840 [293](#), 1814–1818, doi:10.1126/science.1061361.
- 841 Pollitz, F. F. (2003), Transient rheology of the uppermost mantle beneath the Mo-
842 jave Desert, California, *Earth and Planetary Science Letters*, [215](#), 89–104, doi:
843 10.1016/S0012-821X(03)00432-1.
- 844 Pollitz, F. F., G. Peltzer, and R. Bürgmann (2000), Mobility of continental man-
845 tle: Evidence from postseismic geodetic observations following the 1992 Lan-
846 ders earthquake, *Journal of Geophysical Research*, [8035](#)(B4), 8035–8054, doi:
847 10.1029/1999JB900380.
- 848 Pollitz, F. F., R. Bürgmann, and W. Thatcher (2012), Illumination of rheological mantle
849 heterogeneity by the M7.2 2010 El Mayor-Cucapah earthquake, *Geochemistry, Geo-
physics, Geosystems*, [13](#)(6), 1–17, doi:10.1029/2012GC004139.

- Pollitz, F. F. (2015), Postearthquake relaxation evidence for laterally variable viscoelastic structure and water content in the Southern California mantle, *Journal of Geophysical Research: Solid Earth*, **120**, 2672–2696, doi:10.1002/2014JB011603.
- Rauch, H. E., F. Tung, and C. T. Striebel (1965), Maximum likelihood estimates of linear dynamic systems, *AIAA Journal*, **3**(8), 1445–1450.
- Riva, R. E. M., and R. Govers (2009), Relating viscosities from postseismic relaxation to a realistic viscosity structure for the lithosphere, *Geophysical Journal International*, **176**, 614–624, doi:10.1111/j.1365-246X.2008.04004.x.
- Rollins, C., S. Barbot, and J.-P. Avouac (2015), Postseismic Deformation Following the 2010 M7.2 El Mayor-Cucapah Earthquake: Observations, Kinematic Inversions, and Dynamic Models, *Pure and Applied Geophysics*, **172**(5), 1305–1358, doi:10.1007/s00024-014-1005-6.
- Savage, J. C. (1990), Equivalent strike-slip earthquake cycles in half-space and lithosphere-asthenosphere earth models, *Journal of Geophysical Research*, **95**, 4873(B4), 4873–4879, doi:10.1029/JB095iB04p04873.
- Savage, J. C., and J. L. Svart (2009), Postseismic relaxation following the 1992 M-7.3 Landers and 1999 M-7.1 M7.1 Hector Mine earthquakes, southern California, *Journal of Geophysical Research*, **114**(B01401), doi:10.1029/2008JB005938.
- Savage, J. C., J. L. Svart, and S. B. Yu (2005), Postseismic relaxation and transient creep, *Journal of Geophysical Research: Solid Earth*, **110**(B11402), 1–14, doi:10.1029/2005JB003687.
- Segall, P., and M. Mathews (1997), Time dependent inversion of geodetic data, *Journal of Geophysical Research*, **102**, 22391–22409.
- Spinler, J. C., R. A. Bennett, C. Walls, L. Shawn, and J. J. G. Garcia (2015), Assessing long-term postseismic deformation following the M7.2 4 April 2010, El Mayor-Cucapah earthquake with implications for lithospheric rheology in the Salton Trough, *Journal of Geophysical Research: Solid Earth*, **120**, 3664–3679, doi:10.1002/2014JB011613.
- Wei, M., D. Sandwell, Y. Fialko, and R. Bilham (2011a), Slip on faults in the Imperial Valley triggered by the 4 April 2010 Mw 7.2 El Mayor-Cucapah earthquake revealed by InSAR, *Geophysical Research Letters*, **38**(January L01308), 1–6, doi:10.1029/2010GL045235.
- Wei, M., Y. Liu, Y. Kaneko, J. J. McGuire, and R. Bilham (2015), Dynamic triggering of creep events in the Salton Trough, Southern California by regional M5.4 earthquakes constrained by geodetic observations and numerical simulations, *Earth and Planetary Science Letters*, **427**, 1–10, doi:10.1016/j.epsl.2015.06.044.
- Wei, S., E. Fielding, S. Leprince, A. Sladen, J.-P. Avouac, D. Helmberger, E. Hauksson, R. Chu, M. Simons, K. Hudnut, T. Herring, and R. Briggs, (2011b), Superficial simplicity of the 2010 El MayorCucapah earthquake of Baja California in Mexico, *Nature Geoscience*, **4**, 615–618, doi:10.1038/ngeo1213.
- Yang M., and M. N. Toksöz (1981), Time-dependent deformation and stress relaxation after strike-slip earthquakes, *Journal of Geophysical Research*, **86**, 2889–2901.
- Yuen, D. A., and W. R. Peltier (1982), Normal modes of the viscoelastic earth, *Geophysical Journal of the Royal Astronomical Society*, **69**, 495–526, doi:10.1111/j.1365-246X.1982.tb04962.x.